SAND2000-0607J

Visualization of Surfactant Enhanced NAPL Mobilization and Solubilization In a Two-Dimensional Micromodel

Lirong Zhong
Department of Geological Engineering and Sciences
Michigan Technological University

Alex Mayer*
Department of Geological Engineering and Sciences
Michigan Technological University

Robert J. Glass
Flow Visualization and Processes Laboratory
Sandia National Laboratories

*Corresponding author
1400 Townsend Drive
Houghton, Michigan 49931
Phone: (906) 487-3372
Fax: (906) 487-3371
Email: asmayer@mtu.edu

DISCLAIMER

Abstract

Surfactant-enhanced aquifer remediation is an emerging technology for aquifers contaminated with nonaqueous phase liquids (NAPLs). A two-dimensional micromodel and image capture system were applied to observe NAPL mobilization and solubilization phenomena. In each experiment, a common residual NAPL field was established, followed by a series of mobilization and solubilization experiments. Mobilization floods included pure water floods with variable flow rates and surfactant floods with variations in surfactant formulations. At relatively low capillary numbers (N_{ca} <10^{-3}), the surfactant mobilization floods resulted in higher NAPL saturations than for the pure water flood, for similar N_{ca}. These differences in macroscopic saturations are explained by differences in micro-scale mobilization processes. Solubilization of the residual NAPL remaining after the mobilization stage was dominated by the formation of dissolution fingers, which produced nonequilibrium NAPL solubilization. A macroemulsion phase also as observed to form spontaneously and persist during the solubilization stage of the experiments.

INTRODUCTION

Nonaqueous phase liquids (NAPLs) and their component chemicals have become pervasive subsurface groundwater contaminants. Once released into the subsurface, NAPLs migrate downward through the vadose zone towards the water table. Denser-than-water NAPLs, or DNAPLs, penetrate the water table and continue to move downwards into the aquifer, displacing the resident water. Once the bulk volume of the DNAPL release has been exhausted, water re-invades a portion of the aquifer, fragmenting the DNAPL into a series of high saturation pools separated by regions of lower saturation where DNAPL is trapped as residual in discrete ganglia, or blobs, in the pore space.

Conventional DNAPL remediation efforts, such as pump-and-treat, involve increasing the groundwater gradient through the DNAPL-contaminated area. However, impractically large gradients are needed to mobilize trapped DNAPLs. Under typical conditions, the viscous forces imposed by the aqueous phase gradient are not large enough to overcome the high capillary forces that trap the DNAPL in place. These capillary forces are due to the high interfacial tension (IFT) between the DNAPL and aqueous phases. Furthermore, because of the relatively low aqueous solubilities of DNAPLs, large quantities of groundwater are required to completely dissolve the trapped DNAPLs. To address these problems, surfactant-enhanced removal of NAPLs is emerging as an aquifer remediation technology that shows some promise in increasing the efficiency of DNAPL remediation. Surfactant solutions work to mobilize trapped NAPLs by lowering the interfacial tension. Additionally, surfactants enhance the solubilization of entrapped NAPLs in the aqueous phase by incorporating NAPL components into surfactant micelles.

The macro-scale processes affecting DNAPL migration and remediation include immiscible displacement of water by DNAPLs (and vice versa), trapping of DNAPL as pools or residual, mobilization of trapped DNAPL, and DNAPL dissolution or solubilization. Each of these macro-scale processes is controlled by underlying micro-scale physics, where we define the micro-scale as ranging from the single pore to several hundreds or thousands of pores. Most modeling efforts that predict DNAPL migration and dissolution or design systems for remediating DNAPLs are based on macro-scale approaches. However, an understanding of the micro-scale is critical for assessing the accuracy of macro-scale predictions, especially for evaluating innovative remediation technologies. For example, consider the macro-scale nonequilibrium solubilization observed in column experiments by Mayer et al. [1999] for an anionic surfactant-NAPL system. They hypothesized that the observed nonequilibrium behavior is due either to rate limitations in chemical reactions, mass transfer resistance at the NAPL/aqueous interface, or physical phenomena such as bypassing or dissolution fingering, all of which

act at the micro-scale. Determining which micro-scale mechanism is responsible is for the observed macro-scale behavior is critical for proper formulation of models of the solubilization process.

Several experimental methods have been developed to study NAPL distribution, mobilization and dissolution at the micro-scale. Solidification methods rely on introducing NAPLs into the porous media to establish a residual saturation, followed by in situ solidification of NAPL blobs and separation from the porous media [e.g. Conrad et al., 1992; Mayer and Miller, 1992]. Transparent cells filled with a monolayer of glass beads have been used to visualize NAPL distributions at the pore scale [e.g., Mayer and Miller, 1993]. Glass cells etched with idealized pore networks also have been used for NAPL visualization [e.g., Conrad et al., 1992] and to consider mass transfer rates for NAPL dissolution in fresh water [Jai et al. 1999]. In the petroleum industry, such visualization techniques also have been employed to investigate pore-scale, multiphase flow phenomena [e.g., Egbogha and Dawe, 1980; Hornbrook et al., 1991] including a study involving surfactants [Mahers et al., 1981] which considered the influence of aqueous phase flow rates on displacement behavior and blob size and shape distributions. A shortcoming of all these visualization studies has been their qualitative nature.

Recently, methods based on two-dimensional (2D), full-field, quantitative energy transmission techniques [e.g., Tidwell and Glass, 1994] have been developed and applied to increase our understanding of single and two-phase flow and transport processes at both the macro- and micro-scales. These methods have been applied to thin but extensive, heterogeneous sand slabs, where saturation is integrated over the thickness of the slab [e.g., Glass and Nicholl, 1996; Glass et al., submitted]. Additionally, these methods have been applied to 2D transparent micromodel pore networks or fractures where not only can the phase occupancy be quantitatively monitored in time but the pore geometry at the time of the experiment measured with great accuracy and precision. Combining the geometry and phase occupancy allows the detailed quantitative study of a wide range of micro-scale phenomena such as gravity-driven fingering [Nicholl et al., 1993], phase entrapment [Nicholl and Glass, 1994], and entrapped phase dissolution [Glass and Nicholl, 1995].

In the present work, we apply quantitative light transmission techniques to study the micro-scale behavior of surfactant-enhanced NAPL mobilization and solubilization. The objectives of this work are: to visualize surfactant-enhanced NAPL mobilization and solubilization processes; to observe mobilization phenomena and relate their occurrence to system conditions; to observe solubilization phenomena and relate their occurrence to system conditions; and to investigate relationships between macroscopic aqueous phase concentrations and micro-scale solubilization processes.

EXPERIMENTAL DESIGN

We designed experiments to make use of high-resolution, quantitative visualization techniques based on light transmission to measure micromodel pore geometry, phase structure, and phase saturation as a function of time. In each experiment, the water-saturated micromodel was first invaded with NAPL until the phase structure, composed of flowing NAPL and entrapped water, was stable in time. Following this simulated NAPL release, injection was switched to water, thus mobilizing and entrapping NAPL at a residual saturation within the flowing water phase. This residual NAPL structure formed the common starting point for subsequent remediation experiments where surfactant-enhanced NAPL mobilization and solubilization was studied. We designed these enhanced mobilization/solubilization experiments to systematically vary the dimensionless capillary number (N_{ca}) via the interfacial tension between the NAPL and the injected aqueous surfactant solution. Variation in the IFT was produced by changing the chemistry of the surfactant solution, which also produced variation in the NAPL solubility. Another series of mobilization experiments was conducted with pure water floods, where N_{ca} was varied by changing the injection rate of the water.

Experimental System

The experimental system consisted of a transparent micromodel, associated plumbing, and a quantitative light transmission measurement system (see Figure 1(a)). The micromodel chosen was formed by two pieces of roughened glass plate (15 cm x 30 cm) held together with an external fluid pressure of 138 kPa (see Figure 1(b)). This configuration is directly analogous to a rough-walled fracture where similar models have been used extensively in single and two phase flow process studies [e.g., Nicholl and Glass, 1994; Glass and Nicholl, 1995; Nicholl et al., 1999]. However, the micromodel also forms an analog to a 2D granular porous media where the contact points and regions of very small aperture between the two glass plates correspond to the contact points between the grains. The grain contact points, roughly 2-4 correlation lengths apart, are separated by larger gap regions that likewise correspond to the pores within the granular media. We believe this micromodel to be more representative of coarse grained aquifer material than the typical etched and fused plates used by others [e.g., Conrad et al, 1992; Jia et al., 1999].

The micromodel was oriented horizontally and its long sides were sealed with a Viton gasket. At the inflow end of the micromodel, a manifold was installed along the open aperture to distribute fluids evenly. Fluid was delivered to the micromodel from reservoirs weighed continuously on scales to monitor inflow rates. Four syringe needles were installed at the outflow end of the fracture, each connected to one of four independent syringes held in a syringe pump. The syringe pump was used to

pull fluids through the micromodel. This design allowed even outflow from four points at the micromodel edge by eliminating mobilized NAPL blob plugging. Traps were built in each of the four effluent tubing assemblies to capture mobilized NAPL. When mobilized NAPL mixed with aqueous phase passed through the traps, the denser NAPL sank to the bottom and remained in the traps while aqueous phase was withdrawn by the syringe pump. The NAPL level in the traps was monitored and recorded by a video camera. Digital images collected from the video camera were analyzed to determine the cumulative NAPL volume mobilized from the micromodel.

The quantitative light transmission measurement system was composed of a feedback controlled, constant output light table and high-resolution (2048 x 2048 pixels, 4096 gray level), liquid-cooled and shuttered, CCD digital camera (Photometrics). Additional details of this system can be found in Detwiler et al. [1999]. Each pixel of the CCD measured a 0.15 mm by 0.15 mm region of the micromodel. Images of the micromodel were captured at an exposure time of 0.30 seconds with intervals ranging from 15 seconds to 1 hour. Because the NAPL-surfactant solution interactions, such as IFT and solubility, are temperature sensitive, a motorized heat insulating shutter was installed between the micromodel and the light box. All data acquisition and storage procedures were automated, as was most of the experimental system control such as image collection and insulated shutter movement. Conventional cameras and a video recorder also were utilized to collect qualitative, visual information as each experiment progressed.

Fluid solutions and properties

The surfactant solution contained 4% by weight sodium dihexyl sulfosuccinate (Aerosol MA-80I, CYTEC Chemicals, West Paterson, New Jersey) as the surfactant and 4% by weight isopropanol (IPA) as a cosolvent (Aldrich Chemical Co., Milwaukee, Wisconsin). Sodium dihexyl sulfosuccinate is an anionic surfactant with two hydrophobic tails. The surfactant solution also contained various concentrations of NaCl (reagent grade, Aldrich Chemical Co., Milwaukee, Wisconsin): 0.18%, 0.30%, and 0.60% by weight. The aqueous solubilities and the NAPL-aqueous interfacial tensions vary with electrolyte concentration for anionic surfactants such as sodium dihexyl sulfosuccinate. The NAPL used in this study was trichloroethylene (TCE) (99.5+% pure, Aldrich Chemical Co., Milwaukee, Wisconsin) dyed with Oil-red-O (Aldrich Chemical Co., Milwaukee, Wisconsin) at concentration of 0.5 g/L.

Interfacial tensions between TCE and surfactant solutions were measured using a spinning drop tensiometer (Kruss Advancing Rheology & Surface Science, Germany). TCE and surfactant solutions were pre-equilibrated before being injected into the spinning capillary. During all measurements, the temperature of the spinning capillary was controlled at 23.5±0.2°C using an oil bath. A literature value

(IFT = 34.5 dyne/cm) was used for the pure water-TCE IFT [Marcer and Cohen, 1990]. The measured values of IFT between TCE and surfactant solutions and the solubility of TCE in these solutions measured from batch experiments are listed in Table 1. At least 13 sets of IFT measurements were made for each of the surfactant solutions. As expected, as the salt concentration increases, the IFT decreases, and the solubility of TCE increases. The solubilities are from 4 to 10 times the solubility in pure water (approximately 1,100 mg/L).

Experimental Sequence

The experimental sequence for all experiments consisted of four stages: a TCE flood, a water flood, a mobilization flood, and a solubilization flood. The flow was directed along the long axis of the micromodel. The temperature of the micromodel was held at 23.5±0.5°C. The sequence began by saturating the micromodel with water, followed by TCE flooding at a flow rate of 0.2 ml/min. The TCE flood continued until no more water was displaced from the micromodel. Water was then re-introduced to the micromodel at a flow rate of 0.2 ml/min., entrapping the TCE at an initial residual saturation. The water flood continued until TCE was no longer displaced. This sequence produced the common initial point for all of the mobilization/solubilization experiments.

The entrapped NAPL was then mobilized by flushing either with pure water or aqueous surfactant solutions, at a range of velocities and IFTs. Displacement of NAPL blobs occurs when the viscous forces exerted by the invading wetting (aqueous) phase exceeds the capillary forces holding them in place. The dimensionless capillary number (N_{ca}), which relates viscous forces to capillary forces, can be used to quantify the potential for mobilization. The capillary number can be defined as:

$$N_{ca} = \frac{q\,\mu}{\sigma\,\cos\theta} \qquad (1)$$

where q is the Darcy velocity of the displacing fluid, μ is the dynamic viscosity of the displacing fluid, σ is the interfacial tension between aqueous phase and NAPL, and θ is the contact angle of the aqueous phase to the solid material. Capillary desaturation curves typically are used to characterize the mobilization of residual fluids from porous media subjected to viscous floods [Lake, 1989]. These curves relate the remaining residual saturation to the value of N_{ca} estimated for the displacing fluid.

A total of 17 mobilization and solubilization experiments were conducted. Table 2 shows the fluids, average fluid pore velocities and corresponding capillary numbers during each stage of the experiments. When the mobilization was completed, the solubilization stage began and continued until all or most of the remaining residual TCE was solubilized. In the experiments where surfactant floods were used in the

mobilization stage (ten experiments, see Table 2), the same surfactant solution applied during the mobilization stage was used in the solubilization stage. Where pure water was used in the mobilization stage (seven experiments, see Table 2), the micromodel influent was switched from the pure water reservoir to the surfactant solution reservoir at the beginning of the solubilization stage. The range of surfactant formulations used in the solubilization stage (see Table 2) produced a range of TCE solubilities. Some experiments were repeated: experiments TCE-1 and TCE-7; experiments TCE-6 and TCE-15; experiments TCE-4, TCE-5 and TCE-8; experiments TCE-9 and TCE-14, and experiments TCE-11, TCE-12, and TCE-13 were replicates.

The mobilization stages lasted from several minutes to an hour while solubilization stages lasted from several hours to four days. Effluent aqueous samples were collected for two of the experiments during the solubilization stage (experiments TCE-12 and TCE-13). During periods of effluent sampling, an infusion pump was used to deliver liquid to the micromodel through the inflow manifold. Effluent liquids were directed into vials pre-filled with a known amount of water to minimize TCE volatilization and to dilute the effluent samples. An SRI 8610C gas chromatograph (SRI International, Menlo Park, California) with a flame ionization detector was used to determine TCE concentrations.

The micromodel was monitored by digital imaging, video, and conventional camera systems during the complete course of test. The digital image data was processed as described below to provide total NAPL saturations and discrete NAPL blob geometry data. Effluent NAPL volume in the traps was recorded from the beginning of test till the end of mobilization flood. After each experiment, sulfuric acid (18M) with 38 g/L Nochromix was flushed through the micromodel to remove surfactant, residual NAPL, and residual dye. Clean water was then pumped through the micromodel until the effluent pH reached 6.

Measurement of Micromodel Aperture Field and Volume

The micromodel aperture field was measured using light transmission and the protocol of Detwiler et al. [1999]. In this protocol, the aperture field normalized by its mean, is first measured at a series of dye concentrations. Precision and accuracy based error are then assessed to determine the dye concentration that yields the minimum error. The mean aperture is then measured independently and applied to obtain the dimensional aperture field. Using water dyed with FD&C blue #1 (Warner-Jenkinson, St. Louis, Missouri), the minimum error field was found for a dye concentration of 0.06 g/L, yielding a root mean square error of 1.1% of the mean aperture. To obtain the dimensional aperture field, a known volume of water was injected into the initially dry micromodel such that about

three-fourths of the micromodel was filled. The area occupied by water was measured by image analysis using the binarization algorithms described below. The volume divided by area gives the mean aperture in the region occupied by the fluid. Combining the normalized aperture field for the same water-occupied region with this mean aperture yields the dimensional aperture field. Averaging the dimensional aperture field over the entire field yields the mean aperture (0.0998 mm) and the micromodel pore volume (4.68 cm3). Differences in the measurements of the mean aperture before and after all of the experiments were within the measurement error (~0.3%), demonstrating that the micromodel structure did not change significantly over the course of the experiments.

Figure 2 is an image of the aperture field and the aperture distribution. The aperture distribution follows a normal distribution with values ranging up to 0.225 mm, and a standard deviation of 0.028 mm. Spatial correlation lengths were determined from the aperture field using GSLIB [Deutsch and Journel, 1998] as 0.70 mm and 0.82 mm in the short axis and long axis direction, respectively. In Figure 2, we also clearly see large scale heterogeneity within the field that is not captured by the geostatistical analysis. These larger-scale heterogeneities, on the scale of about one-third of the micromodel width (~5 cm), superimpose a slight undulating structure on top of the smaller scale random field. For example, consider the two regions at the bottom of micromodel designated in Figure 3. One region represents an area with larger apertures (predominately white) and the other region represents an area with smaller apertures (predominately black). The region with larger apertures has a mean aperture size that is 23% greater than the full-field mean, while the mean aperture size in the region with smaller apertures is 5% lower than the full-field mean.

To demonstrate the influence of the aperture field heterogeneity on the fluid flow, a dye solution was pumped through the micromodel at a pore velocity of 0.022 cm/s. Shown in Figure 3 are images of the dye solution flush at two different times with and without NAPL at a residual saturation of 12%, which is a typical saturation at the end of the mobilization stage of the experiments. These figures show the two scales of variability in the flow characteristics. The larger scale variability (on the order of centimeters) is demonstrated by the three dye "fingers" that are ahead of the average position of the dye front. The smaller scale variability (on the order of millimeters) is demonstrated by the finer fingers distributed around the larger scale variability. In addition, a comparison of Figures 3(a) and (b) with 3(e) and (f) shows that the residual NAPL has a negligible influence on the large scale flow pattern at this low saturation. However, at the higher saturations typical of the end of the water flood stage, the occurrence of residual NAPL is very important in defining the aqueous flow structure, as has been demonstrated previously by Nicholl and Glass [1994].

Experimental Image Processing and Measurement of NAPL Saturation and Blob Geometry

The image processing scheme is shown in Figure 4. The first step is to adjust the gray levels in each image to compensate for slight temporal fluctuations in light source intensity. A light transmitting wedge with a range of constant density steps was installed next to the micromodel and included in each experimental image in order to monitor the intensity of the source. Small fluctuations in transmitted light intensity are removed by adjusting intensities of experimental images to those in a reference image. After gray level adjustment, images were corrected for slight shifts caused by occasional vibrations of the test stand to a tolerance of 0.05 of a pixel. Further details on gray level adjustment and shifting can be found in Detwiler et al., [1999].

The differences in transmitted light intensity between NAPL and aqueous phases were used to transform raw images to binary phase distribution images where each pixel occupied by either NAPL or aqueous phase is represented by a 1 or 0, respectively. The light transmitted through the micromodel varies over the entire field, especially near the cell edges. Thus, a single threshold intensity value cannot be used to binarize the entire field. Instead, we use the adaptive thresholding technique where a local histogram is employed to define a local threshold for binarization [Nicholl and Glass, 1994]. The percent distance between the local peaks for NAPL and water is chosen for a given field to best match the binarized and raw images by eye. An approximately 0.5-cm swath along the edges of the micromodel was excluded from the binarized field, and thus the saturation estimates, because the transparent gasket for the confinement gas chamber disturbed the light transmission at its inner edge. The excluded area was 9.8% of the total micromodel area.

The product of the binarized phase structure and the aperture field, summed over the image, yields the NAPL volume within the image. Dividing this volume by the total image volume yields the NAPL saturation. The binarized images of trapped NAPL were also used for blob size and shape measurement. The blob area, perimeter, and length were measured using Clemex Vision software (Clemex Technologies, Canada). The blob length was defined as the direction of the largest span of a blob in the average flow direction (the long dimension of the micromodel).

The accuracy of binarization impacts both the total phase saturation and NAPL blob geometry measurements. In order the evaluate the possible error in these measurements, we chose the distance between the NAPL and water peaks in the binarization algorithm to be slightly higher and lower than that found to give the best binarization by eye. Each of these distances were chosen to yield a small but noticeable over- and under-estimate of the area occupied by the NAPL, yielding a deviation in total

saturation of 3% and in the mean blob length of 2%. These differences are considered to represent the possible maximum error of the image based measurements. To further assess the accuracy of NAPL saturation measurement by image processing, the total saturations obtained through image processing were compared with those based on a total volume balance using inflow and outflow trap data. The average, absolute difference between the mean S_n based on image processing and the mean S_n based on volume balance after the TCE flood is 0.6% and after the water flood is 1.9%, both well within measurement error.

RESULTS AND DISCUSSION

In the following, we describe the results for each of the experimental stages. The NAPL distributions after the water flood are described first. This stage provided the common initial condition for the mobilization experiments, which are described next. The NAPL saturations and distributions after mobilization by the pure water and surfactant floods are analyzed and compared. Finally, the fluid phase behavior during the solubilization stage of the experiments is described.

NAPL Distribution Prior to Mobilization and Solubilization Stages

TCE saturations in the micromodel after TCE floods and water floods are listed in Table 2. The mean TCE saturation was 59.2% with a standard deviation of 2.5%, and 41.6% with a standard deviation of 3.1% after the TCE floods and the water floods, respectively. The outlier TCE saturation (experiment TCE-05) was caused by an aberrantly high flow rate at the beginning of the TCE flood. Example NAPL structures after the TCE and water floods from three experiments are shown in Figure 5. These images show that the complex NAPL structure is controlled not only by small scale heterogeneities in the aperture field, but also by heterogeneities at the larger scale identified earlier in the aperture field measurements and dye displacement experiments (see Figures 2 and 3). NAPL is consistently found at higher saturations in regions of larger average mean aperture, both after the TCE flood and the water flood, yielding a base phase structure that is similar from experiment to experiment. However, we also see that while the structures following each of the floods are similar and that the saturations are nearly the same, there are small differences in the phase structure.

Table 3 lists the geometric mean and standard deviation of blob length in the direction of average flow (the long side of the micromodel) for each experiment, following the water flood and prior to the mobilization stage. The pooled arithmetic mean and pooled arithmetic standard deviations among the

geometric means and standard deviations also are given in Table 3. The results in Table 3 indicate that there is significant variability among the blob size distributions prior to the mobilization stage. Furthermore, there is a trend towards smaller blob sizes in time across the experimental set (i.e., as the experiment number increases). This trend is likely due to an increase in the effective contact angle (from water-wetting towards NAPL-wetting conditions) as the micromodel aged during the course of the experiments. Increases in the effective angle can be caused by roughening of the glass surface due to etching by the acid solutions used to clean the glass, or alternatively, by the contamination of the glass surface by residual materials over time.

With regard to the influences of these small variations in initial conditions on the 'remediation' stage presented below, comparison of replicate experiments for both water and surfactant floods show no apparent correlation between the initial conditions, as characterized by NAPL saturations and/or blob size statistics, and the saturations and/or blob size statistics following mobilization.

Mobilization of residual NAPL

Shown in Figure 6 are images of the phase structure midway through the water and surfactant mobilization floods. For the water flood (Figure 6(a)), NAPL movement occurs simultaneously over the entire aperture field and forms a series of long "rivulets" oriented in the direction of flow. Alternatively, in surfactant floods, a visible front of high NAPL saturation forms (Figures 6(b)-(d)) that sweeps the entire width of the cell. The images in Figures 6(b)-(d) suggest that, as the IFT between the surfactant solution and NAPL decreases, the tendency to form a concentrated front increases.

Close inspection of the evolving phase structure during water floods shows that blobs first stretch in the downstream direction and combine with other stretching blobs to form rivulets. At the trailing edge of individual stretched mobilized blobs, we find snap-off and shedding of entrapped blobs at a smaller size than in the initial field. The development of rivulets usually extends to previously NAPL-free areas, especially when capillary numbers for water mobilization are large. Rivulet formation throughout the field prevents the formation of a front. The extension of blobs in the direction of flow also was observed by Wardlaw and McKellar [1985] in a column packed with glass beads, where larger blobs fissioned repeatedly upon mobilization, resulting in the re-entrapment of the smaller daughter blobs. In our case, the extension of blobs was greater and more frequent than that observed by Wardlaw and McKellar [1985], resulting in larger numbers of re-entrapped, smaller daughter blobs.

Inspection of the phase structure during surfactant floods shows that as the surfactant moves into the residual NAPL field, mobilization is restricted to a narrow zone with the NAPL downstream of the front completely undisturbed. As this zone moves further into the field, mobilized NAPL from behind the

surfactant front congregates to form the high saturation NAPL front. The congregation and subsequent formation of the front strengthens as the IFT decreases. Behind the mobilization front, the NAPL field is composed of small blobs that are nearly uniformly distributed within the micromodel. Interestingly, at the leading edge of the front, we also find NAPL to migrate upstream against the mean direction of flow and contribute to the formation of the mobilization front. Figure 7 shows a sequence of images from experiment TCE-08; the arrows indicate the migration of a portion of a blob occurring in the countercurrent direction. This upstream migration is caused by a capillary force imbalance within the blob, due to an up to two order of magnitude difference in IFTs between the upstream and downstream edges of the blob.

Images of trapped NAPL after mobilization are presented in Figure 8 for a range of capillary numbers. All images show the same region within the micromodel. We see in Figure 8, that for both water floods (images (a), (b), (c), and (e)) and surfactant floods (images (d), (f), (g), and (h)), the trapped TCE blobs become smaller and less complicated as N_{ca} increases. Blob length distributions for water and surfactant floods are shown in Figures 9(a) and (b), respectively. The figures indicate that both the mean length and the variation in lengths decrease as the N_{ca} increase. We also see that at similar N_{ca}, the blob length distribution curves are similar for water floods and surfactant floods; for example, the distribution for the water flood at $N_{ca} = 1.1 \times 10^{-3}$ is similar to the distribution for the surfactant flood at $N_{ca} = 1.2 \times 10^{-3}$. The maximum blob length and the geometric mean blob length are plotted versus N_{ca} in Figure 10. Both the maximum and geometric mean blob length display an approximately inverse relationship with N_{ca} with no apparent difference between the water and surfactant floods. This inverse relationship is suggested by simple force balances as presented by Mayer and Miller [1992] for porous media or Longino and Kueper [1999] for fractures.

While the geometric characteristics of the individual blobs is independent of the "path" taken during mobilization, i.e., water vs. surfactant flood, the average saturation after mobilization will be path-dependent because of the very different mechanisms that act during the mobilization process. In water floods, the rivulet formation tends to leave a more sparsely filled blob field, while the mobilization front that forms during surfactant floods will sweep the entire domain width and leave NAPL behind in every pore that is not excluded by viscous forces. This observation is supported by the results shown in Figure 8 where the number of entrapped blobs after surfactant floods is higher than that after water floods at similar N_{ca} (Figure 8, (c) vs. (d), (f) vs (g)). In Figure 11, the number of entrapped blobs within the micromodel is plotted as a function of N_{ca}. The results in Figure 11 indicate that for a similar N_{ca}, a significantly higher number of blobs is obtained in surfactant floods than that in water floods, when $N_{ca} < 10^{-3}$.

These differences in blob numbers between water and surfactant floods translate directly into differences in average saturation. As shown in Figure 12, a significantly higher residual saturation is obtained with surfactant floods for a given N_{ca}, when $N_{ca} < 10^{-3}$. According to current conceptual models, the residual NAPL saturation following mobilization should scale to the capillary number, for a given pore structure. That is, the same residual saturation should be reached for a specified N_{ca}. However, we find clear differences in residual TCE saturation due to the different underlying mechanisms of front versus rivulet formation between water and surfactant mobilizations and thus a "path" dependence. We note that this discrepancy between water and surfactant floods is far beyond what can be attributed to our error in determining N_{ca} or the saturations. Furthermore, if our implicit assumption that the contact angles are zero for both the water and surfactant floods is incorrect, this error would not explain the magnitude of the difference between the water and surfactant desaturation results. The general trends in the capillary desaturation curves shown in Figure 12 are similar to those found in the literature [e.g., Lake, 1989], where the majority of the nonwetting phase is displaced for $N_{ca} > 10^{-3}$ and complete displacement occurs at about $N_{ca} = 10^{-2}$. Mahers et al. [1981] present capillary desaturation curves for high and low IFT mobilization floods. The results of Mahers et al. [1981] do not indicate any significant difference in trends of saturation vs. N_{ca} between the high and low tension floods; however their experiments were conducted over a more narrow range of N_{ca} than the results given here.

Solubilization of residual NAPL

Shown in Figure 13 are images of the solubilization flood at increasing pore volumes from experiments TCE-01, TCE-06, TCE-10, and TCE-11. The formation and propagation of dissolution fingers (clear areas) can be observed in these images. Dissolution fingering is a result of instabilities that develop at the solubilization front [e.g., Imhoff et al., 1996]. As the fingers propagate through the field, three fingers typically grow faster than the others, become dominant, and eventually break through the effluent end of the micromodel. The locations of the three dominant fingers correspond to the preferential flow zones where the velocity was shown to be higher in the dye transport experiment (Figure 3). The influence of solubilization capacity of surfactant solutions and initial NAPL saturations is also demonstrated in Figure 13. When other conditions are held constant, the dissolution fingers develop and propagate faster when the solubility is higher (TCE-06 versus TCE-01). When the solubility is held constant, the fingers grow and propagate faster when the initial NAPL saturation is lower (TCE-06 > TCE-10 > TCE-11). These results, demonstrating the influence of the permeability field,

solubility, and NAPL saturation are all in agreement with the observations of Imhoff et al. [1996] in pure water/NAPL systems.

Plotted in Figure 14 are the mass removal rates, normalized by the solubilization rate that would occur under equilibrium conditions, for the same experiments as shown in Figure 13. The number of pore volumes associated with dissolution finger breakthrough at the end of the micromodel are depicted in this figure for each experiment. During the early stages of the solubilization experiments, the NAPL removal rates are higher than the equilibrium rate in three of the four experiments, indicating that some NAPL mobilization was occurring. After the early stage and before finger breakthrough, the NAPL removal rates are at or close to the equilibrium solubilization rate. After finger breakthrough, the normalized mass removal rates decrease considerably. Figure 15 shows the effluent TCE concentration measured in aqueous samples normalized by the equilibrium concentration for experiment TCE-13. The normalized effluent TCE concentration assuming equilibrium conditions is given in the figure for comparison purposes. Images of the fingers at the outflow edge of the micromodel for the associated pore volumes flushed are also shown. Equilibrium concentrations were reached between one and two pore volumes (PV) and remain relatively constant until about 20 PV. Effluent concentrations are again seen to decrease with the breakthrough of dissolution fingers.

These results illustrate that, for the flow velocities and NAPL-surfactant system used in this study, observations of macro-scale nonequilibrium are associated with dissolution fingering, rather than a chemical rate limitation or a mass transfer resistance. The dissolution fingering produces the observed nonequilibrium behavior because the portion of the aqueous phase flowing through the clear fingers (where the NAPL has been eliminated) has dissolved NAPL concentrations significantly below equilibrium (solubility) levels. The remaining portion of the aqueous phase flow occurs in areas containing residual NAPL, where one would expect the dissolved NAPL concentrations to be near or at equilibrium, given sufficient residence time. Thus, the width-averaged dissolved NAPL concentration yields an observed nonequilibrium behavior.

During several of the solubilization experiments, the spontaneous formation of a translucent or gray phase was observed in the micromodel. Figure 16 shows the occurrence of the gray phase (dark gray areas) in experiment TCE-01, along with aqueous phase (white to light gray areas) and residual NAPL (black blobs). The gray phase is most likely a macroemulsion, consisting of small, light-scattering droplets of NAPL surrounded by surfactant molecules suspended in the aqueous phase. Macroemulsions usually are considered to be unstable, meaning that the NAPL droplets should eventually coalesce. However, once the macroemulsion formed in the micromodel, it persisted, indicating that the time

required for coalescence of the NAPL droplets in this system is longer than the residence time of the macroemulsion in the micromodel.

The macroemulsion appeared in areas where the local NAPL saturation was relatively high, as indicated by the absence of the macroemulsion in the upgradient portion of the micromodel in Figure 16, where the majority of the NAPL has been solubilized. In addition, the macroemulsion was not observed inside the dissolution fingers, as is also shown in Figure 16. This observation implies that the formation and persistence of the macroemulsion depends on saturation, a dependency that also was reported by Okuda et al. [1996] in batch NAPL-surfactant experiments. In the case of the micromodel solubilization experiments, the local saturation dependency is related to the availability of NAPL to sustain the high dissolved concentration required to form suspended macroemulsions in the aqueous phase.

Occurrence of the macroemulsion also is correlated with the surfactant formulation. As the salt concentration increased, the formation and persistent of the macroemulsion decreased. This result could be explained by either of two factors. First, the spontaneous formation of the macroemulsion may be prevented, or at least minimized, at high salt concentrations due to the change in electrolyte chemistry in the aqueous solution. Second, higher salt concentrations result in reduced interfacial tensions and consequently lower residual saturations following the mobilization stage. Thus, the reduced occurrence of the macroemulsion at higher salt concentrations could simply be due to the coincidentally reduced NAPL saturations within the micromodel.

Macroemulsion formation and persistence could have a significant impact on solubilization rates because a mobile macroemulsion phase would be capable of transporting apparent concentrations of NAPLs that are considerably higher than solubility concentrations. We did not observe concentrations significantly higher than solubility in the micromodel effluent when macroemulsion was present; however, effluent concentrations were measured in only two of the experiments where macroemulsions were observed. Macroemulsions also can have the effect of increasing the mobile fluid viscosity, which would in turn reduce the aqueous phase permeability [Okuda et al., 1996]. We did not measure the viscosity of the macroemulsion phase directly; however, we did not observe any significant variations in aqueous phase flow patterns when the macroemulsion was present, as compared to cases where the macroemulsion occurrence was reduced or absent.

CONCLUSIONS

A micromodel and quantitative visualization system were applied to observe surfactant-enhanced NAPL mobilization and solubilization phenomena at the micro-scale. The micromodel consisted of two plates of textured glass held in contact, producing a series of variably-sized, connected apertures available for fluid flow. The quantitative visualization system was capable of resolving micromodel aperture geometry and the evolution of NAPL phase structure and saturation. For each experiment, a common residual NAPL field was established with a NAPL flood into the water saturated micromodel followed by a water flood at low flow rates. We then conducted a series of mobilization/solubilization experiments where the chemical formulation of the flood was varied from pure water to floods containing an anionic surfactant and cosolvent at fixed concentrations and a range of electrolyte concentrations. The variations in the electrolyte concentrations provided a range of IFTs and NAPL solubilities. For the surfactant floods, the flow rate was kept at the same rate used to establish the residual NAPL, yielding a final N_{ca} modified only by changes in the IFT. For the pure water floods, the flow rate was varied to modify the N_{ca} by changes in viscous forces alone.

For a given N_{ca}, we found significant differences in the macro-scale saturation at the end of the mobilization stage of the experiments, for $N_{ca} < 10^{-3}$. The observed differences occur because the changes in the local N_{ca} during the surfactant floods occurs through a miscible displacement process, while during pure water floods, changes in the local N_{ca} are established immediately throughout the field. This path dependency, i.e., changes in the local N_{ca} via increases in viscous forces or via miscible IFT reduction, is in turn caused by differences in micro-scale processes. For the surfactant floods, a high NAPL saturation front forms normal to the direction of flow and sweeps the entire field width. The IFT reduction fronts form due to the combination of N_{ca}-induced downstream and capillary-driven upstream mobilization processes. For the water floods, rivulets oriented in the direction of flow form and are driven downstream. Rivulet formation occurs through the simultaneous application of viscous forces in primarily a single direction throughout the field. These very different, path-dependent, micro-scale processes between the surfactant and pure-water floods lead to a difference in final macro-scale saturation. The differences in saturation are attributed to differences in the number of remaining, entrapped NAPL blobs, rather than differences in final blob size statistics.

Solubilization of the residual NAPL remaining after the mobilization stage was dominated by the formation of dissolution fingers. The fingers developed and propagated faster at lower residual NAPL saturations and when the aqueous phase solubility was higher. The location of finger initiation and propagation was directly related to spatial heterogeneity in the aperture field. Equilibrium NAPL mass

removal rates were observed before the dissolution fingers broke through the effluent edge of the micromodel. Following finger breakthrough, the solubilization rate decreased below the rate expected if equilibrium solubilization were occurring throughout the micromodel and continued to decline as the back of the dissolution finger zone advanced to the downstream boundary. Thus, at the flow rates and chemical formulations considered in our experiments, macro-scale nonequilibrium NAPL solubilization can be attributed directly to the development of a dissolution finger zone where significant heterogeneity occurs due to micro-scale dissolution fingering.

A macroemulsion phase was observed to form spontaneously and persist during portions of the solubilization stage of the experiments. The occurrence of the macroemulsion was related directly to local NAPL saturation, where macroemulsion formation was found to be more likely at higher local NAPL saturations, and was at least indirectly related to electrolyte concentration in the surfactant formulation. The impact of macroemulsion on solubilization rates is unclear, since micromodel effluent concentrations and aqueous phase flow patterns did not appear to be affected by macroemulsion occurrence.

ACKNOWLEDGMENTS

This work has been funded by the U.S. Environmental Protection Agency ORD/NCERQA, Grant Agreement #R824505-01-0 at Michigan Technological University and the U.S. Department of Energy's Basic Energy Science Geoscience Program and Environmental Management Science Program at Sandia National Laboratories. Experiments were conducted in the Flow Visualization and Processes Laboratory at Sandia National Laboratories. We thank William J. Peplinski and Donald Fox for assistance in modifying and setting up the experimental system and data processing procedures.

REFERENCES

Conrad, S. H., Wilson, J. L., Mason, W. R., and Peplinksi, W. J., Visualization of Residual Organic Liquid Trapped in Aquifers, *Water Resources Research*, 28(2), 467--478, 1992.

Detwiler, R.L., Pringle, S.E. and Glass, R.J., Measurement of Fracture Aperture Fields Using Transmitted Light: An Evaluation of Measurement Errors and Their Influence on Simulations of Flow and Transport through a Single Fracture, *Water Resources Research*, 35 (9), 2605-2617, 1999.

Deutsch, C. V. and Jurnel, A. G., GSLIB Geostatistical Software Library and User's Guide, second edition, Oxford University Press, 1998.

Egbogah, E. O. and Dawe, R. A., Microvisual Studies of Size Distribution of Oil Drops in Porous Media, *Bulletin of Canadian Petroleum Geology*, 28, 200-210, 1980.

Glass, R. J. and Nicholl, M. J., Quantitative Visualization of Entrapped Phase Dissolution Whin a Horizontal Flowing Fracture, *Geophysical Research Letters*, 22, (11) 1413-1416, 1995.

Glass, R. J. and M. J. Nicholl, Physics of gravity driven fingering of immiscible fluids within porous media: An overview of current understanding and selected complicating factors, *Geoderma*, 70:133-163, 1996.

Glass, R. J., S. H. Conrad, and W. Peplinski, Gravity destabilized non-wetting phase invasion in macro-heterogeneous porous media: Experimental Observations of Invasion Dynamics and Scale Analysis, submitted to *Water Resources Research*, 1999.

Hornbrook, J. W., Castanier, L. M., and Pettit, P. A., Observation of Foam Oil Interactions in a New High-Resolution Micromodel, in *The 66th Annual Technical Conference and Exhibtion of SPE*, SPE paper number 22631, Dallas, TX, 1991.

Imhoff, P. T., Thyrum, G. P., and Miller, C., Dissolution Fingering During the Dissolution of Nonaqueous Phase Liquids in Saturated Media 2. Experimental Observations, *Water Resources Research*, 32(7)1929-1942, 1996.

Jia, C., Shing K. and Yortsos, Y.C., Visualization and Simulationof Non-aqueous Phase Liquids Solubilization in Pore Networks, *Journal of Contaminant Hydrology*, 25, 363-387, 1999.

Lake, L., *Enhanced Oil Recovery*, Prentice Hall, Englewood Cliffs, New Jersey, 1989.

Longino, B. L. and Kueper.B.H., Nonwetting Phase Retention and Mobilization in Rock Fractures, *Water Resources Research*, 35, 2085-2093, 1999.

Mahers, E. G., Wright, R. J., and Dawe, R. A., Visualization of the Behavior of EOR Reagents in Displacements in Porous Media, in Enhanced Oil Recovery, *Proceedings of the Third European Symposium on Enhanced Oil Recovery*, edited by Fayer, F. J., Elsevier Scientific Publishing Co., Amsterdam, 1981.

Marcer, J. W. and Cohen, R. M., A Review of Immiscible Fluid in the Subsurface: Properties, Models, Characterization and Remediation, *Journal of Contaminant Hydrology*, 6, 107-163, 1990.

Mayer, A. S. and Miller, C. T., An Experimental Investigation of Pore-Scale Distribution of Nonaqueous Phase Liquids at Residual Saturation, *Transport in Porous Media*, 1057-85, 1993.

Mayer, A. S. and Miller, C. T., The Influence of Porous Media Characteristics and Measurement Scale on Pore-Scale Distributions of Residual Nonaqueous Phase Liquids, *Journal of Contaminant Hydrology,* 11, 189-213, 1992.

Mayer, A. S., Zhong, L., and Pope, G. A, Measurement of Mass Transfer Rate for Surfactant-Enhanced Solubilization of Nonaqueous Phase Liquids, *Environmental Science and Technology*, 33, 2965-2972, 1999.

Nicholl, M. J., Glass, R. J., and Nguyen, H. A Small-scale behavior of single gravity driven fingers in an initially dry fracture, *Proc. 4th Int. Conf. of High Level Rad. Waste Manage.*, American Nuclear Society, April 26-30, Las Vegas, NV, pp 2023-2033, 1993.

Nicholl, N. J. and Glass, R. J., Wetting Phase Permeability in a Partially Saturated Horizontal Fracture, in *Proceedings of the Fifth Annual International High Level Radioactive Waste Management Conference*, Am. Nuc. Soc., 1994.

Nicholl, N. J., H. Rajaram, R. J. Glass, and R. Detwiler, Saturated flow in a single fracture: Evaluation of the Reynolds Equation in Measured Aperture Fields, in press, *Water Resources Research.*

Okuda, I., Mcbride, J. F., Gleyzer, S. N., and Miller, C. T., Physicochemical Transport Process Affecting The Removal of Residual NAPL by Nonionic Surfactant Solutions, *Environmental Science and Technology,* 30, 1852-1860, 1996.

Tidwell, V.C., and R.J. Glass, X-ray and visible light transmission for laboratory measurement of two dimensional saturation fields in thin slab systems. *Water Resources Research*, 30, 2873-2882, 1994.

Wardlaw, N. C. and McKellar, M., Oil Blob Populations and Mobilization of Trapped Oil in Unconsolidated Packs, *The Canadian Journal of Chemical Engineering*, 63, 525-532, 1985.

Table 1. Interfacial Tension and Solubility Results

Surfactant Formulation	Mean IFT (dyn/cm)	Standard Deviation in IFT (dyn/cm)	Solubility (ppm)
1.6% MA~4.0% IPA~0.18% NaCl	0.95	0.12	3920
1.6% MA~4.0% IPA~0.30% NaCl	0.62	0.08	5080
1.6% MA~4.0% IPA~0.60% NaCl	0.23	0.01	9950

Table 2. Summary of Experiments

Experiment No.	TCE Flood		Water Flood		Mobilization Stage				Solubiliz. Stage	
	v * (cm/s)	S_n (%)	v (cm/s)	S_n (%)	v (cm/s)	Composition **	N_{ca}	S_n (%)	v (cm/s)	Composition **
TCE-01		55.3		42.6	0.020	surf./0.18% NaCl	2.9E-4	35.0		surf./0.18% NaCl
TCE-02		58.1		43.1	0.020	surf./0.30% NaCl	4.2E-4	27.6		NA****
TCE-03		57.7		43.0	0.020	surf./0.30% NaCl	4.2E-4	30.9		NA****
TCE-04		60.0		39.1	0.020	surf./0.60% NaCl	1.2E-3	15.4		surf./0.60% NaCl
TCE-05		65.7		46.9	0.020	surf./0.60% NaCl	1.2E-3	9.6		surf./0.60% NaCl
TCE-06		57.0		40.6	0.020	surf./0.30% NaCl	4.2E-4	35.5		surf./0.30% NaCl
TCE-07		60.1		42.3	0.020	surf./0.18% NaCl	2.9E-4	37.1		surf./0.18% NaCl
TCE-08	v =	59.9	v =	46.2	0.020	surf./0.60% NaCl	1.2E-3	16.9	v =	surf./0.60% NaCl
TCE-09	0.022	59.3	0.022	45.9	0.112	pure water	4.0E-5	36.5	0.020	surf./0.30% NaCl
TCE-10		60.1		38.9	0.55	pure water	2.0E-4	22.3		surf./0.30% NaCl
TCE-11		57.8		38.4	2.75	pure water	1.0E-3	14.6		surf./0.30% NaCl
TCE-12		59.5		43.6	2.75	pure water	1.0E-3	15.2		surf./0.30% NaCl
TCE-13		62.2		42.9	2.75	pure water	1.0E-3	18.6		surf./0.30% NaCl
TCE-14		56.6		36.9	0.112	pure water	4.0E-5	28.5		surf./0.30% NaCl
TCE-15		57.5		37.7	0.020	surf./0.30% NaCl	4.2E-4	29.4		surf./0.30% NaCl
TCE-16		61.9		42.0	0.414	surf./0.30% NaCl	7.9E-3	0.4		surf./0.30% NaCl
TCE-17		57.7		37.8	5.50	pure water	2.0E-3	14.0		surf./0.30% NaCl
Mean		59.2		40.1						
Std. Dev.**		2.5		3.1						

*v = pore velocity

**surf.: surfactant solution, where all solutions include the indicated NACL concentration by weight, 1.6% MA-80I surfactant by weight and 4.0% IPA by weight

***Std. Dev.: standard deviation

****NA: Solubilization stage not performed for this experiment

Table 3. NAPL Blob Lengths Following Water Flood

Experiment No.	Geometric Mean (mm)	Geometric Standard Deviation (mm)
TCE-01	1.73	3.05
TCE-02	1.83	2.51
TCE-03	1.76	2.58
TCE-04	1.52	2.33
TCE-05	1.92	2.68
TCE-06	1.88	2.61
TCE-07	1.66	2.61
TCE-08	1.62	2.48
TCE-09	1.50	2.50
TCE-10	1.56	2.48
TCE-11	1.41	2.44
TCE-12	1.30	2.51
TCE-13	1.54	2.53
TCE-14	NM*	NM
TCE-15	1.49	2.39
TCE-16	1.48	2.65
TCE-17	1.33	2.34
Average	1.60	2.54
STDEV	0.19	0.17

* not measured

FIGURE CAPTIONS

Figure 1. Schematic of experimental system.

Figure 2. Image of the aperture field and frequency distribution of aperture sizes. The gray scale in the image indicates the aperture size. The two rectangular regions at the bottom of micromodel show the maximum and minimum undulation in the field.

Figure 3. Visualization of the flow field. Images show the flow pattern at different pore volumes of dye solution flushed: images (a) and (b) are from a dye test without trapped NAPL; images (c) and (d) are from a dye test with trapped NAPL; and images (e) and (f) are images where the trapped NAPL has been subtracted from images (c) and (d), respectively. Direction of flow in left-to-right in images.

Figure 4. Image processing procedure.

Figure 5. Comparison of NAPL distributions following TCE floods and water floods for three experiments. Direction of flow in left-to-right in images.

Figure 6. Images of the mobilization front: (a) water flood, IFT = 32 dyn/cm, $v = 2.75$ cm/s, $N_{ca} =$ 1.0E-3 (TCE-11); (b) surfactant flood, IFT = 0.98 dyn/cm, $v = 0.020$ cm/s, $N_{ca} = 2.9E\text{-}4$ (TCE-01); (c) surfactant flood, IFT = 0.68 dyn/cm, $v = 0.020$ cm/s, $N_{ca} = 4.2E\text{-}4$ (TCE-03); and (d) surfactant flood, IFT = 0.23 dyn/cm, $v = 0.02$ cm/s, $N_{ca} = 1.2E\text{-}4$ (TCE-05). Direction of flow is from left-to-right in images.

Figure 7. Series of images demonstrating the migration of NAPL blobs (right to left) against the average direction of flow (left to right) in experiment TCE-08. Arrows point to the location of the upstream migration. Images (a) through (d) were captured at 15 seconds time intervals. The area of the micromodel in the image is 6.5 by 4.5 cm. Direction of flow is from left-to-right in images.

Figure 8. Images of NAPL blobs following mobilization as a function of capillary number and flood type. All images show the same region in the micromodel and have a size of 250 by 400 pixels (3.8 cm by 6.1 cm). NAPL and aqueous phase are white and black, respectively. Direction of flow is from left-to-right in images.

Figure 9. NAPL blob size distributions following mobilization flood (a) water mobilization flood and (b) surfactant mobilization flood.

Figure 10. Maximum (a) and geometric mean (b) blob lengths in the average direction of flow as a function of capillary number.

Figure 11. Number of blobs vs. capillary number following mobilization. Each symbol represents averages over replicate experiments. Error bars indicate one standard deviation from the mean, where replicate experiments were conducted.

Figure 12. Capillary desaturation for water mobilization and surfactant mobilization floods. Symbols represent averages over replicate experiments. Error bars in the y-axis direction represent one standard deviation for residual NAPL saturations from the replicate experiments. Error bars in the x-axis direction represent the uncertainty in the capillary number associated with the IFT measurements (one standard deviation).

Figure 13. Influence of initial NAPL saturation on solubilization and formation of dissolution fingers. The NAPL saturation corresponding to each image is given at the top of the image. The axis at the bottom of the figure indicates the number of pore volumes fed corresponding to the images above the axis. Direction of flow is from left-to-right in images.

Figure 14. NAPL mass removal rate normalized by the rate that would occur during equilibrium conditions vs. number of pore volumes fed as a function of starting NAPL saturation. Arrows indicate the number of pore volumes fed corresponding to finger breakthrough for each experiment.

Figure 15: Normalized effluent TCE concentration (dashed lines and symbols) and residual saturation (dashed line) vs. number of pore volumes fed for experiment TCE-12. The solid line represents the effluent concentration expected if equilibrium conditions were occurring. Attached are images (15 by 13.5 cm) of the outflow edge of the micromodel for the corresponding number of pore volumes. Direction of flow is from left-to-right in images.

Figure 16. Macroemulsion occurrence during solubilization in experiment TCE-01. The white areas in the images are regions of clear aqueous phase, the black areas are NAPL blobs, and the gray areas are aqueous surfactant solution with macroemulsion. Direction of flow is from left-to-right in images.

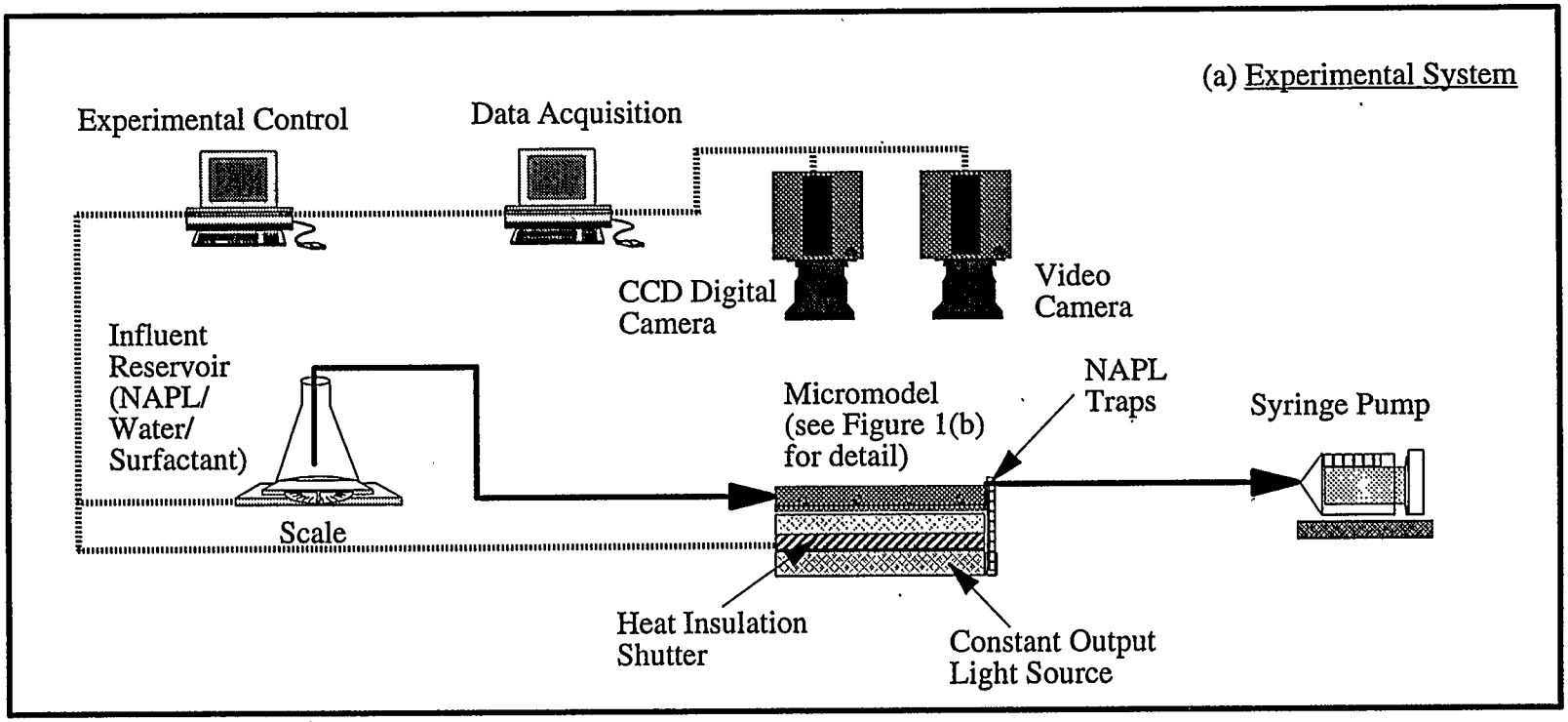
(a) Experimental System
Experimental Control
Data Acquisition
CCD Digital Camera
Video Camera
Influent Reservoir (NAPL/ Water/ Surfactant)
Scale
Micromodel (see Figure 1(b) for detail)
NAPL Traps
Syringe Pump
Heat Insulation Shutter
Constant Output Light Source

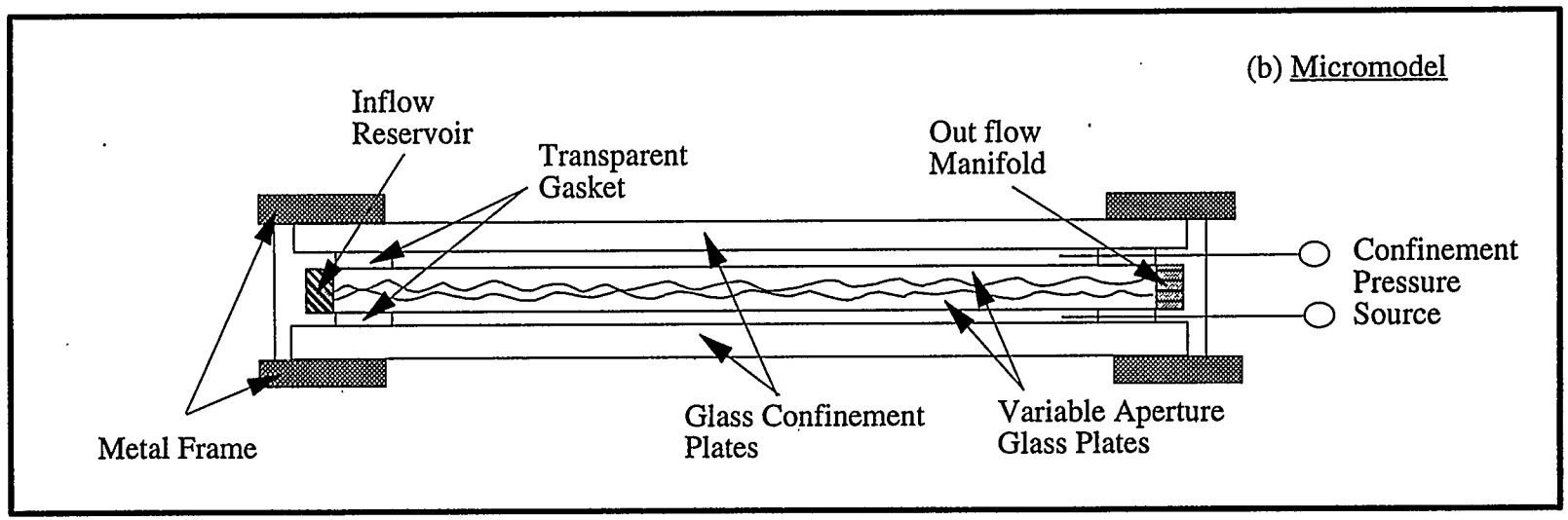
(b) Micromodel
Inflow Reservoir
Transparent Gasket
Out flow Manifold
Confinement Pressure Source
Metal Frame
Glass Confinement Plates
Variable Aperture Glass Plates

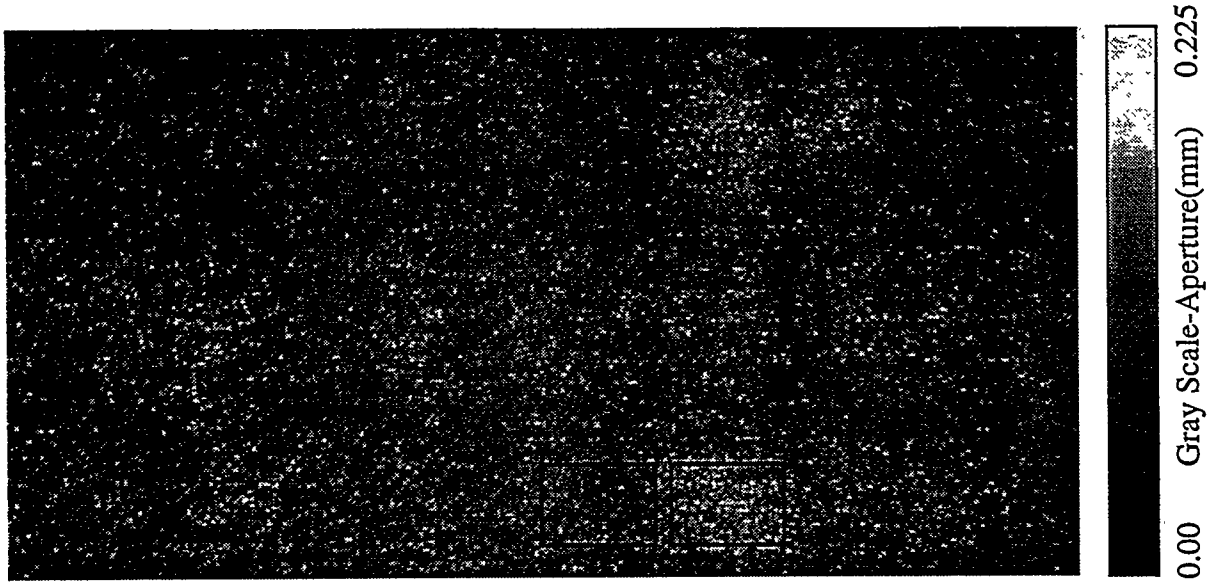
0.225
Gray Scale-Aperture(mm)
0.00

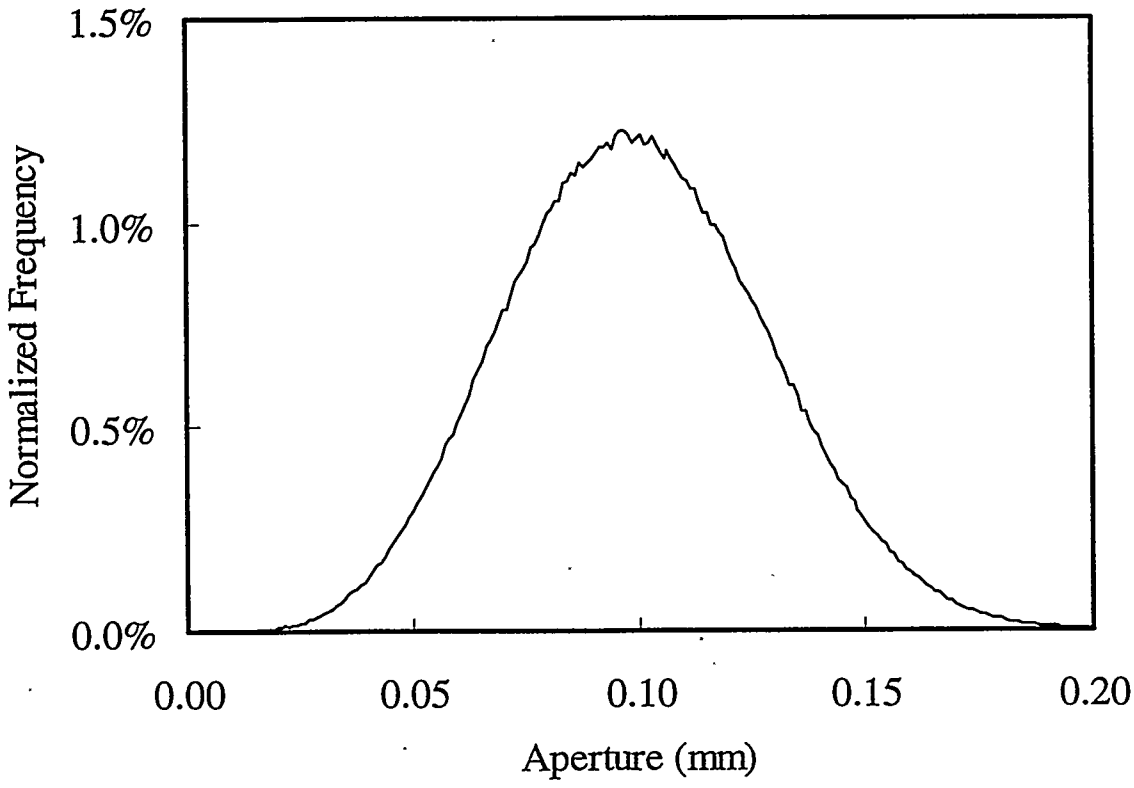
1.5%
1.0%
0.5%
0.0%
Normalized Frequency
0.00
0.05
0.10
0.15
0.20
Aperture (mm)

Fig. 2

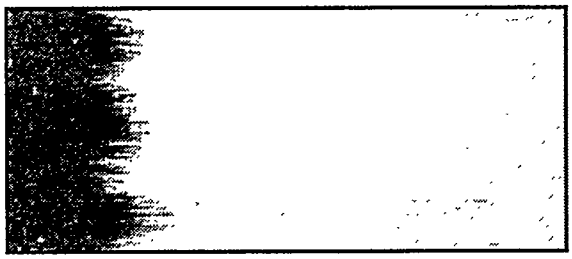

(a) 0.25 PV

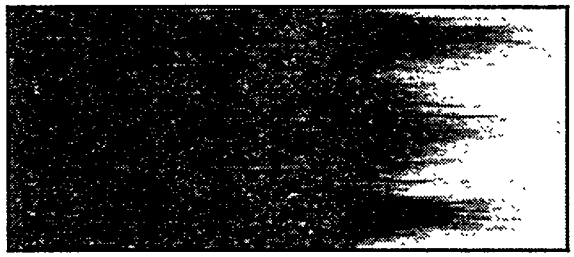

(b) 0.81 PV

(c) 0.13 PV

(d) 0.64 PV

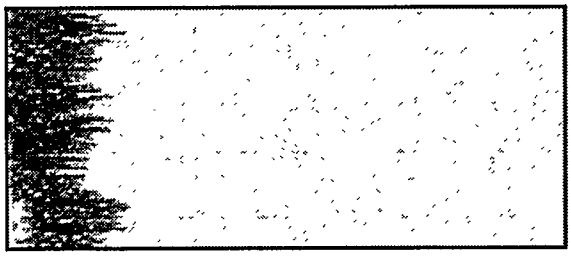

(e) 0.13 PV

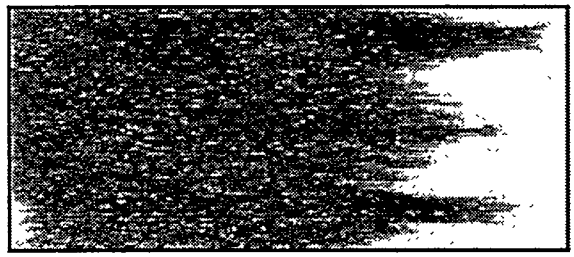

(f) 0.64 PV

Fig. 3

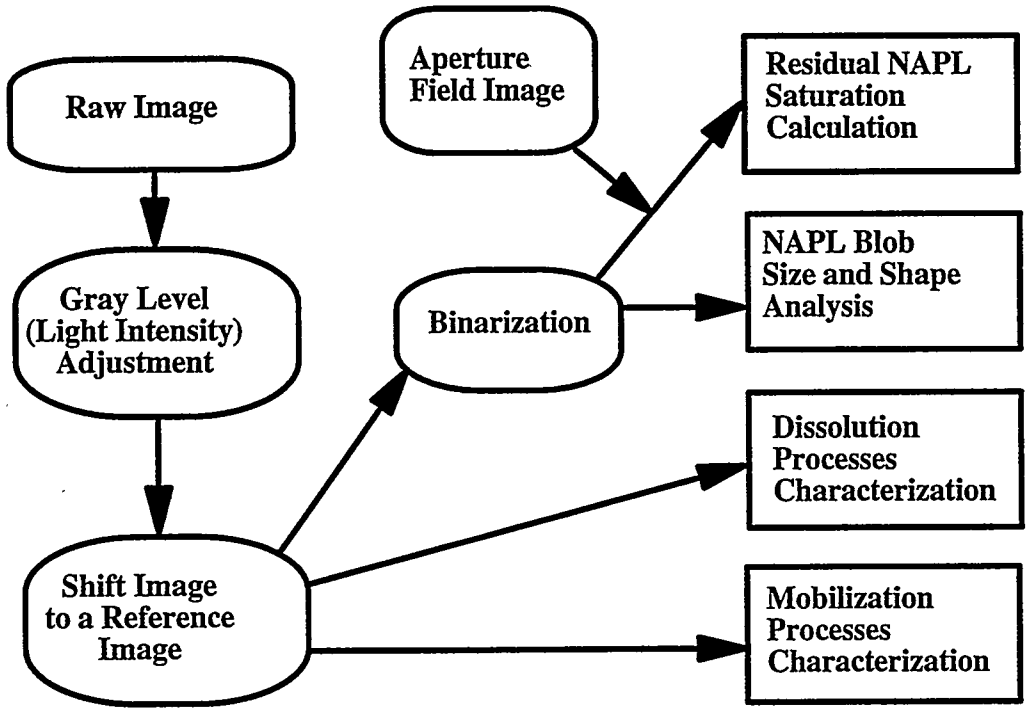
Raw Image
Gray Level (Light Intensity) Adjustment
Shift Image to a Reference Image
Aperture Field Image
Binarization
Residual NAPL Saturation Calculation
NAPL Blob Size and Shape Analysis
Dissolution Processes Characterization
Mobilization Processes Characterization

After TCE Flood

After Water Flood

Experiment TCE-01

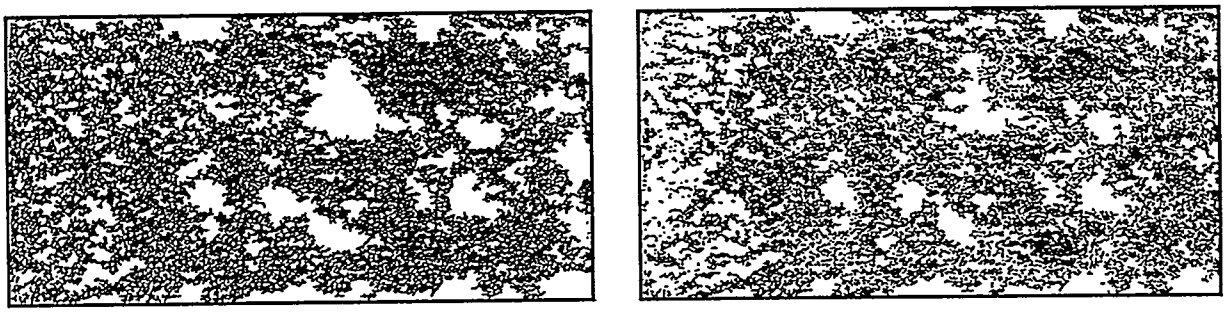

Experiment TCE-03

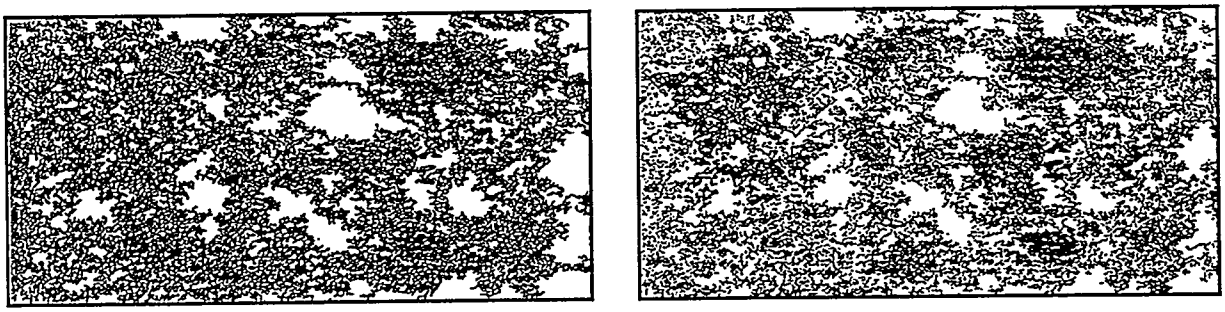

Experiment TCE-08

Fig. 5

(a)

(b)

(c)

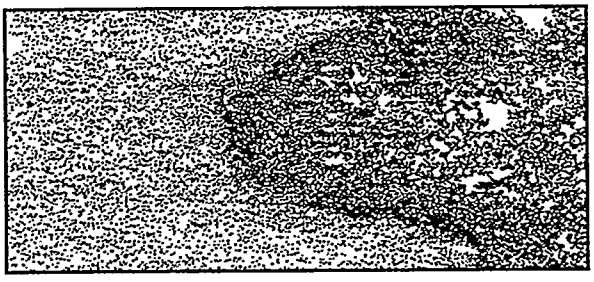

(d)

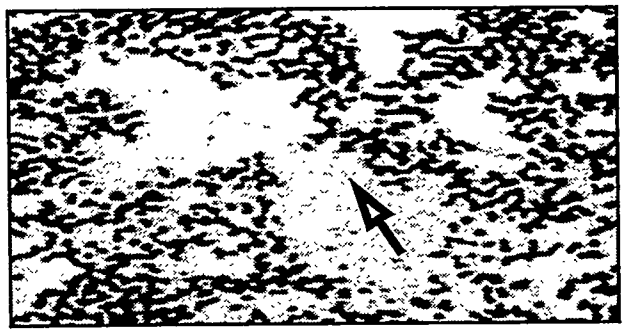

(a)

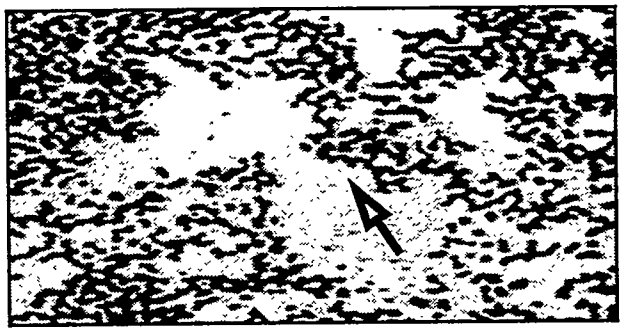

(b)

(c)

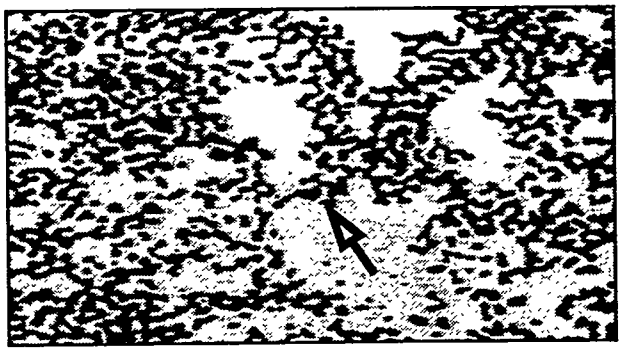

(d)

Fig. 7

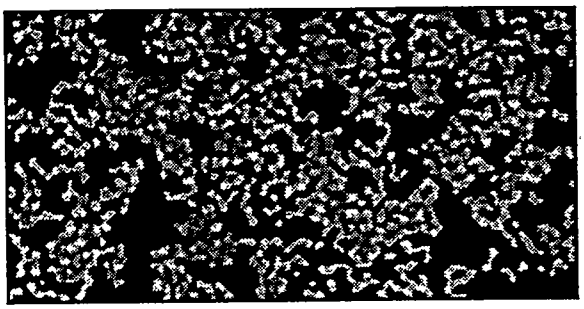

(a). N_{ca}=8.1E-6, Water

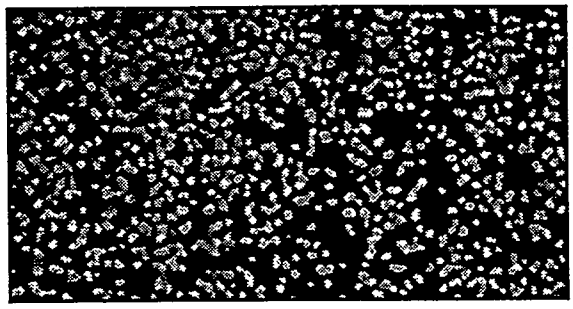

(e)E. N_{ca}=4.2E-4, Surfactant

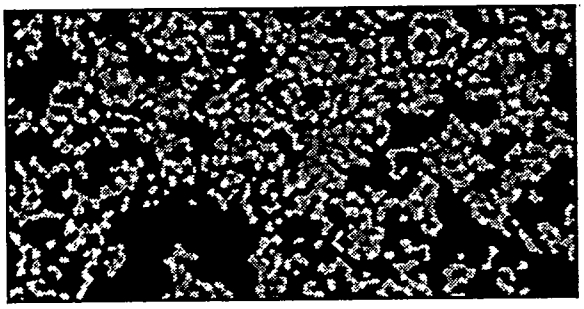

(b). N_{ca}=4.0E-5, Water

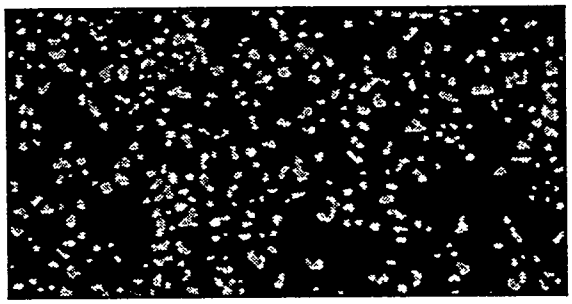

(f). N_{ca}=1.0E-3, Water

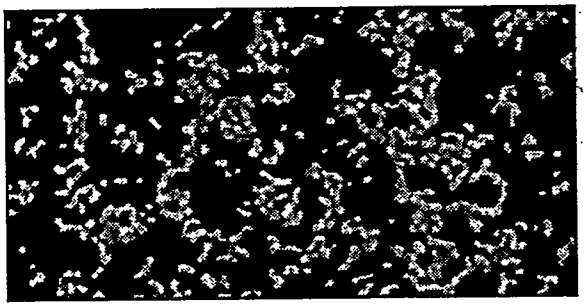

(c).N_{ca}=2.0E-4, Water

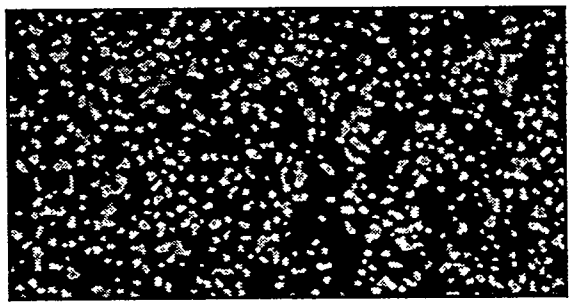

(g). N_{ca}=1.2E-3, Surfactant

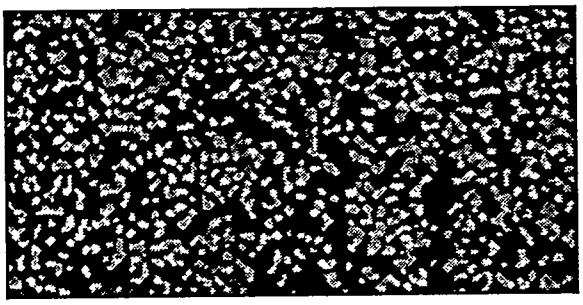

(d). N_{ca}=2.9E-4, Surfactant

(h). N_{ca}=7.9E-3, Surfactant

Fig. 8

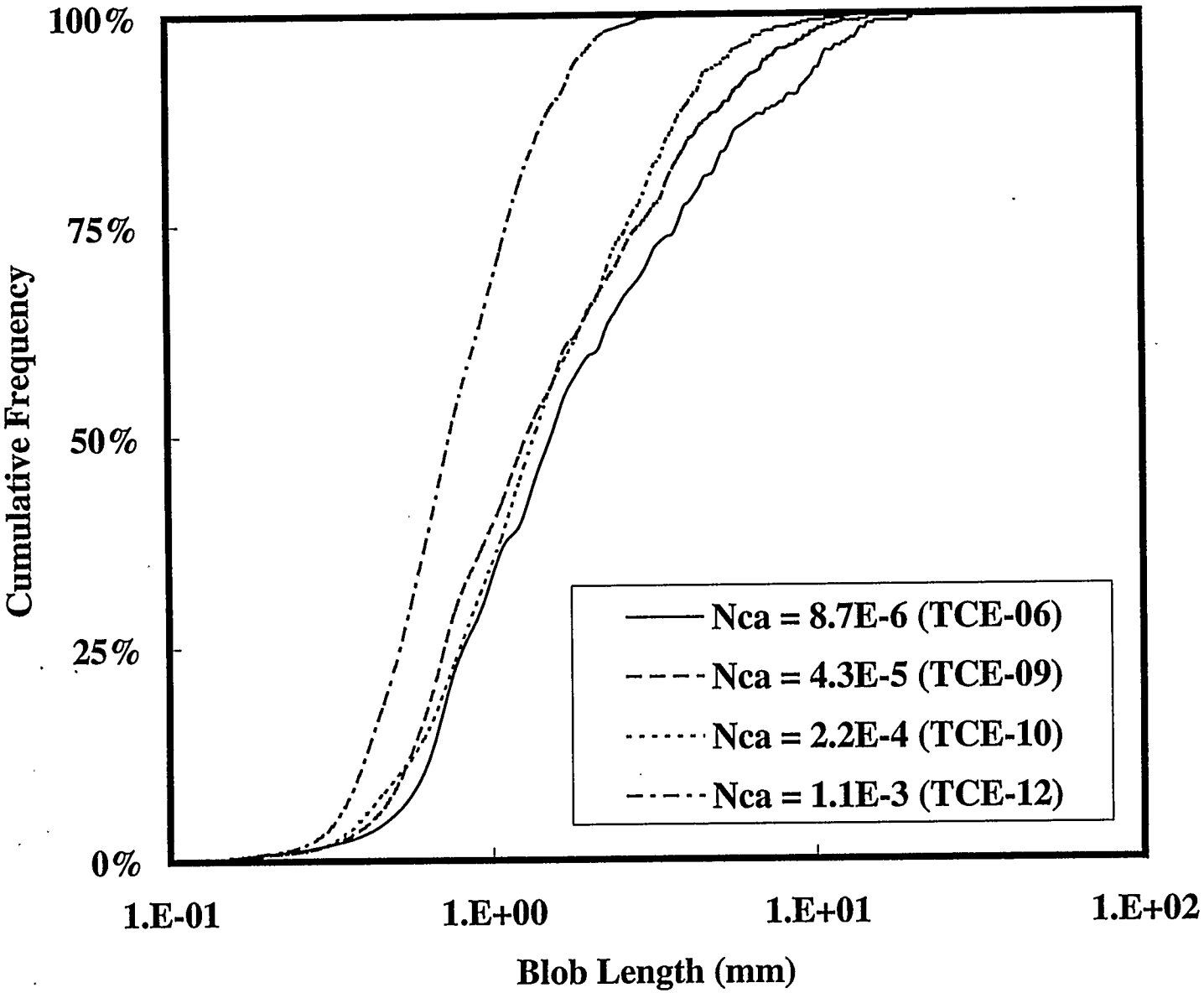
100%
75%
50%
25%
0%
Cumulative Frequency
1.E-01
1.E+00
1.E+01
1.E+02
Blob Length (mm)
Nca = 8.7E-6 (TCE-06)
Nca = 4.3E-5 (TCE-09)
Nca = 2.2E-4 (TCE-10)
Nca = 1.1E-3 (TCE-12)

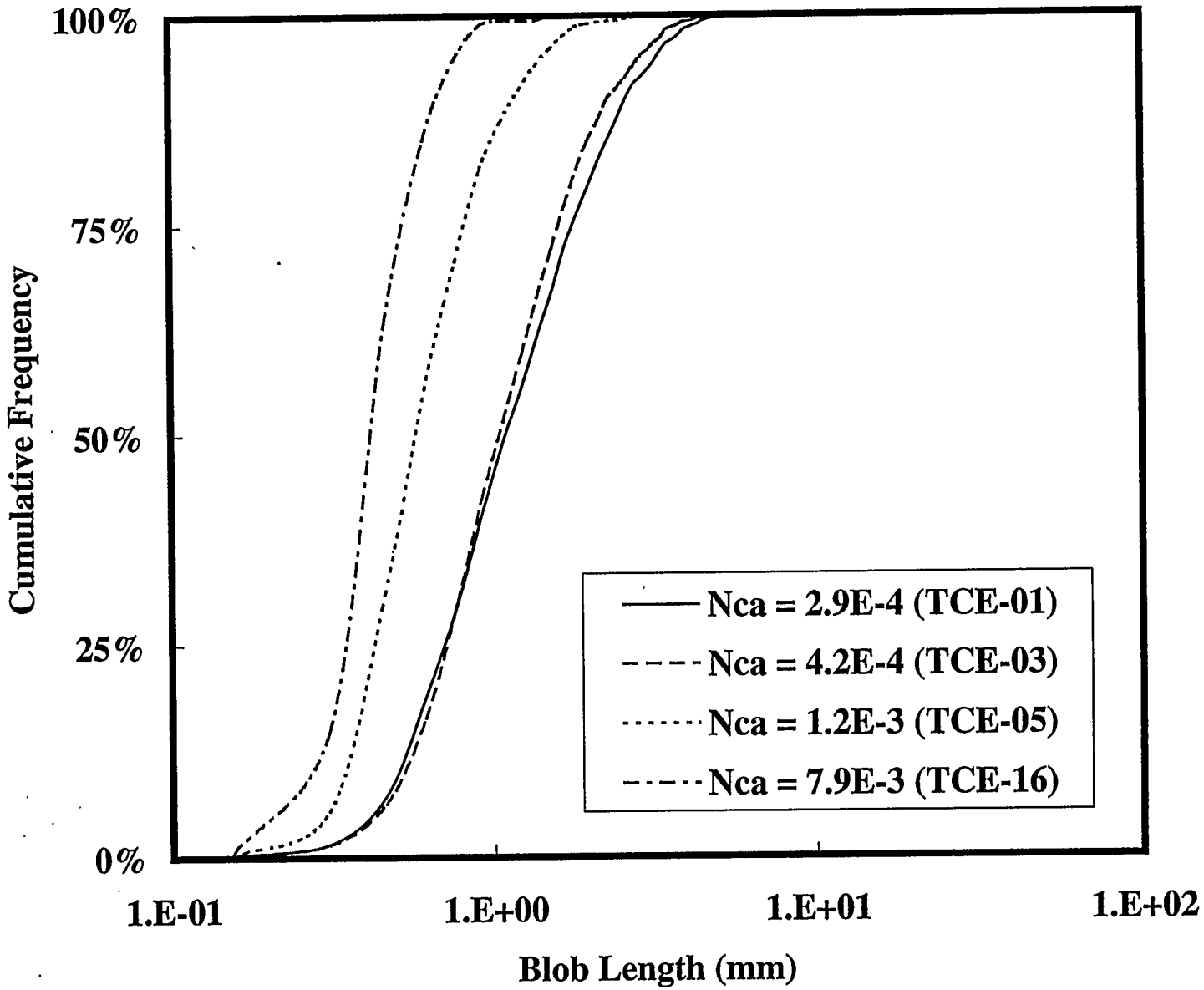
100%
75%
50%
25%
0%
Cumulative Frequency
1.E-01
1.E+00
1.E+01
1.E+02
Blob Length (mm)
Nca = 2.9E-4 (TCE-01)
Nca = 4.2E-4 (TCE-03)
Nca = 1.2E-3 (TCE-05)
Nca = 7.9E-3 (TCE-16)

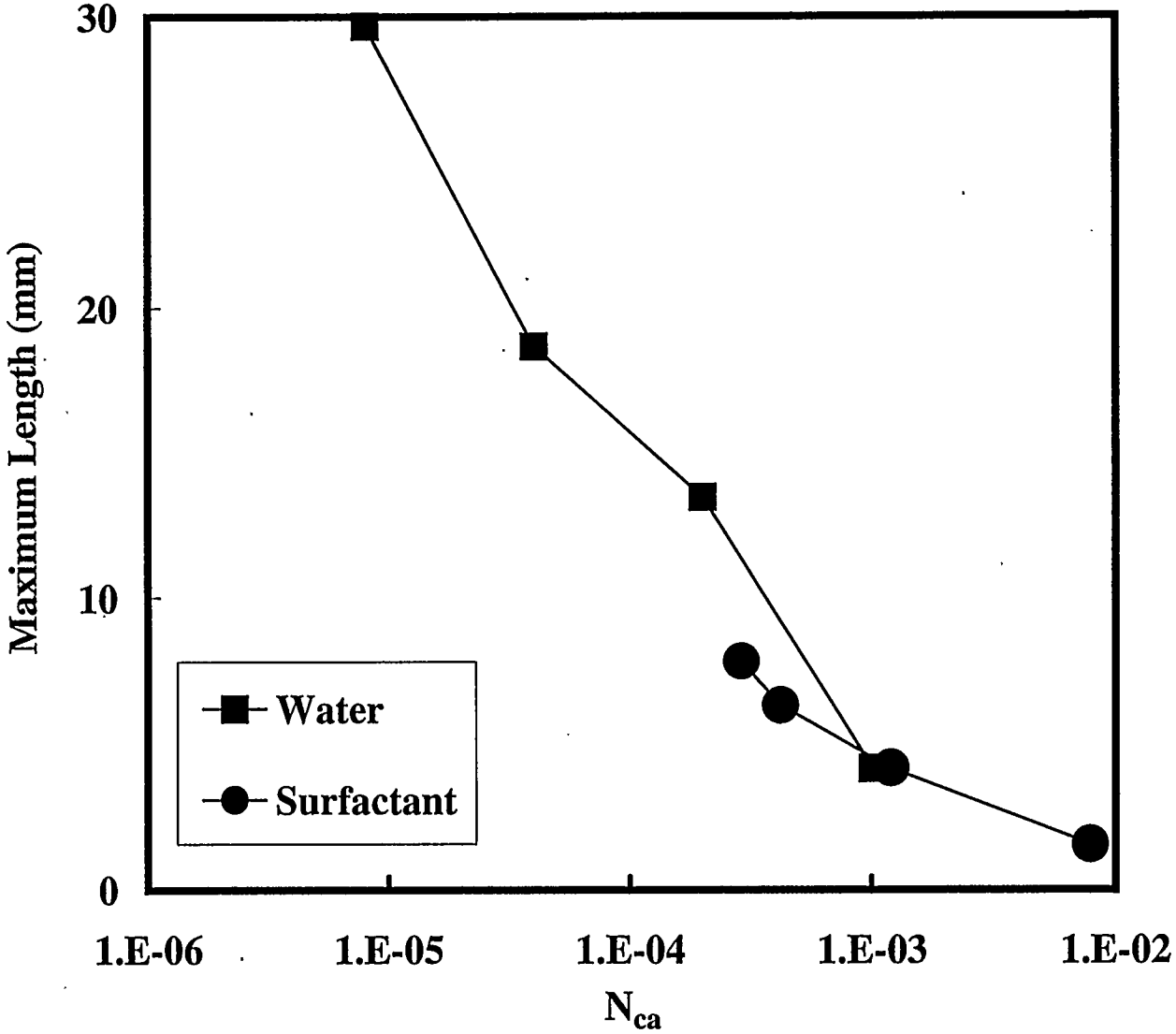
30
20
10
0
Maximum Length (mm)
Water
Surfactant
1.E-06
1.E-05
1.E-04
1.E-03
1.E-02
N_{ca}

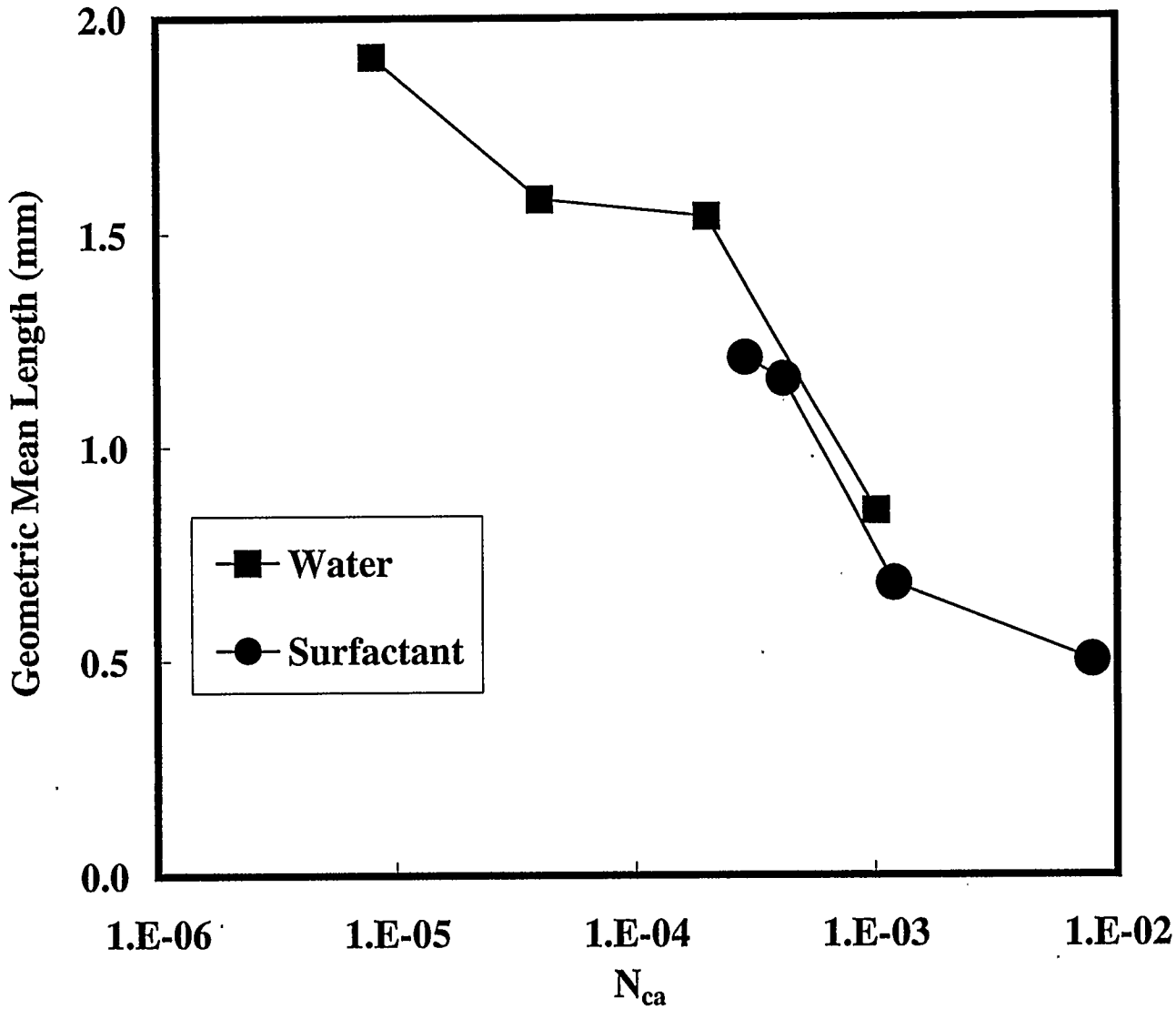
2.0
1.5
1.0
0.5
0.0
Geometric Mean Length (mm)
Water
Surfactant
1.E-06
1.E-05
1.E-04
1.E-03
1.E-02
N_{ca}

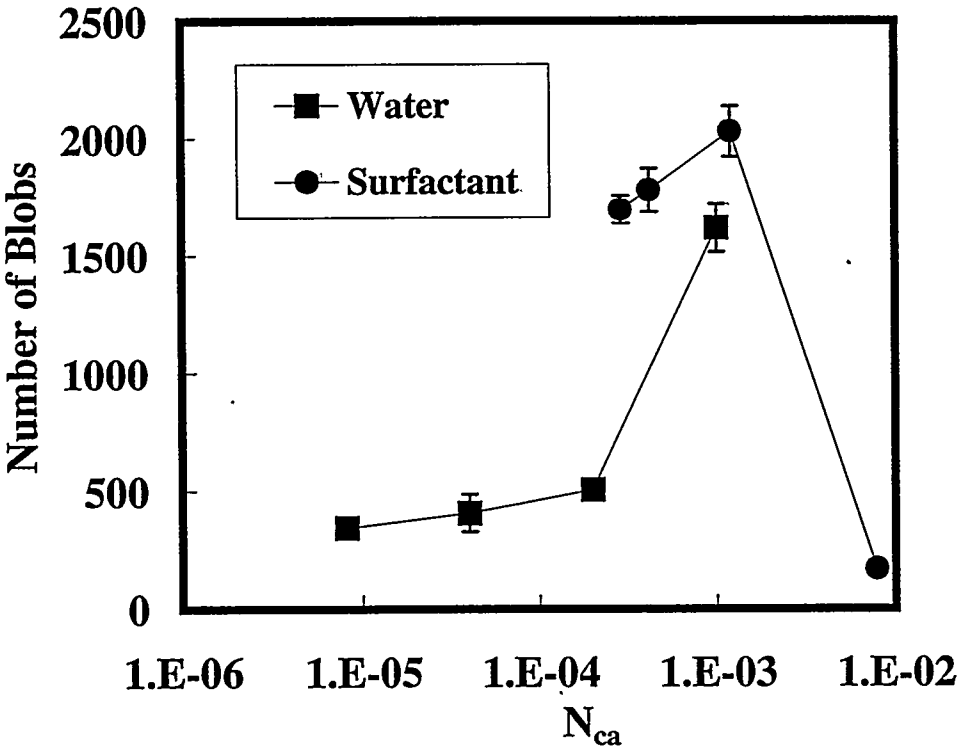
2500
2000
1500
1000
500
0
Number of Blobs
Water
Surfactant
1.E-06
1.E-05
1.E-04
1.E-03
1.E-02
N_{ca}

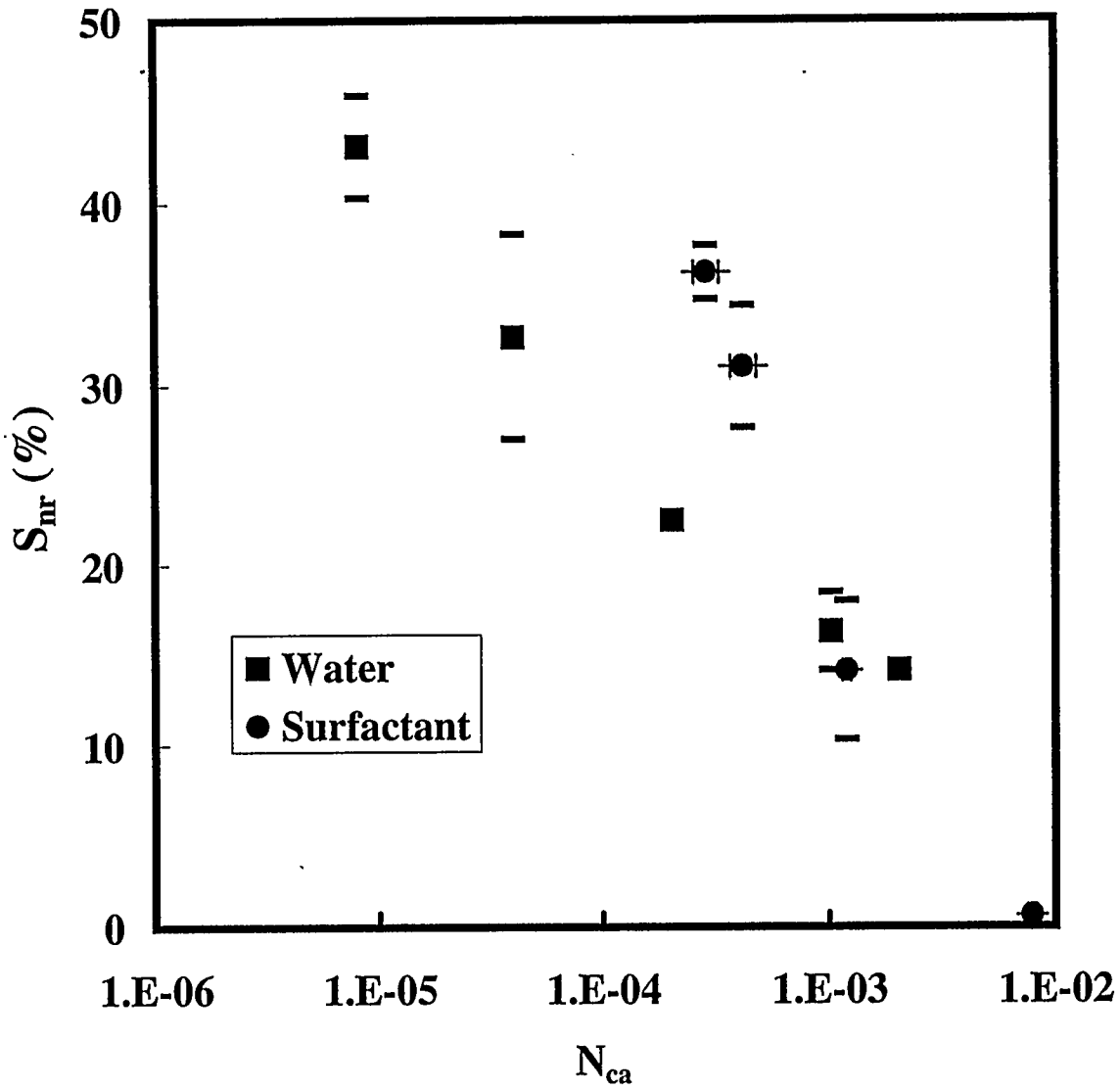
50
40
30
20
10
0
S_{nr} (%)
Water
Surfactant
1.E-06
1.E-05
1.E-04
1.E-03
1.E-02
N_{ca}

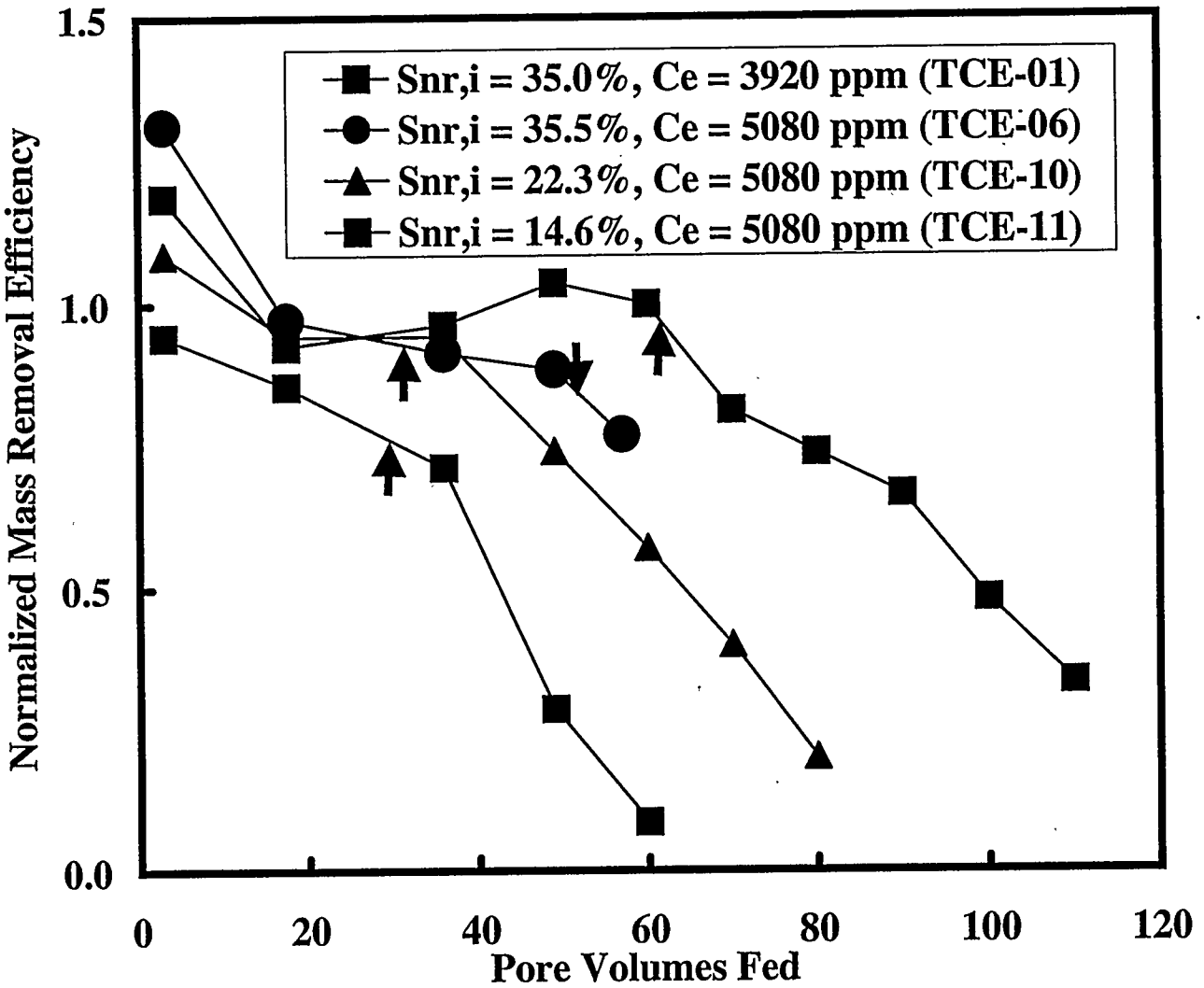
Snr,i = 35.0%, Ce = 3920 ppm (TCE-01)
Snr,i = 35.5%, Ce = 5080 ppm (TCE-06)
Snr,i = 22.3%, Ce = 5080 ppm (TCE-10)
Snr,i = 14.6%, Ce = 5080 ppm (TCE-11)
Normalized Mass Removal Efficiency
1.5
1.0
0.5
0.0
0
20
40
60
80
100
120
Pore Volumes Fed

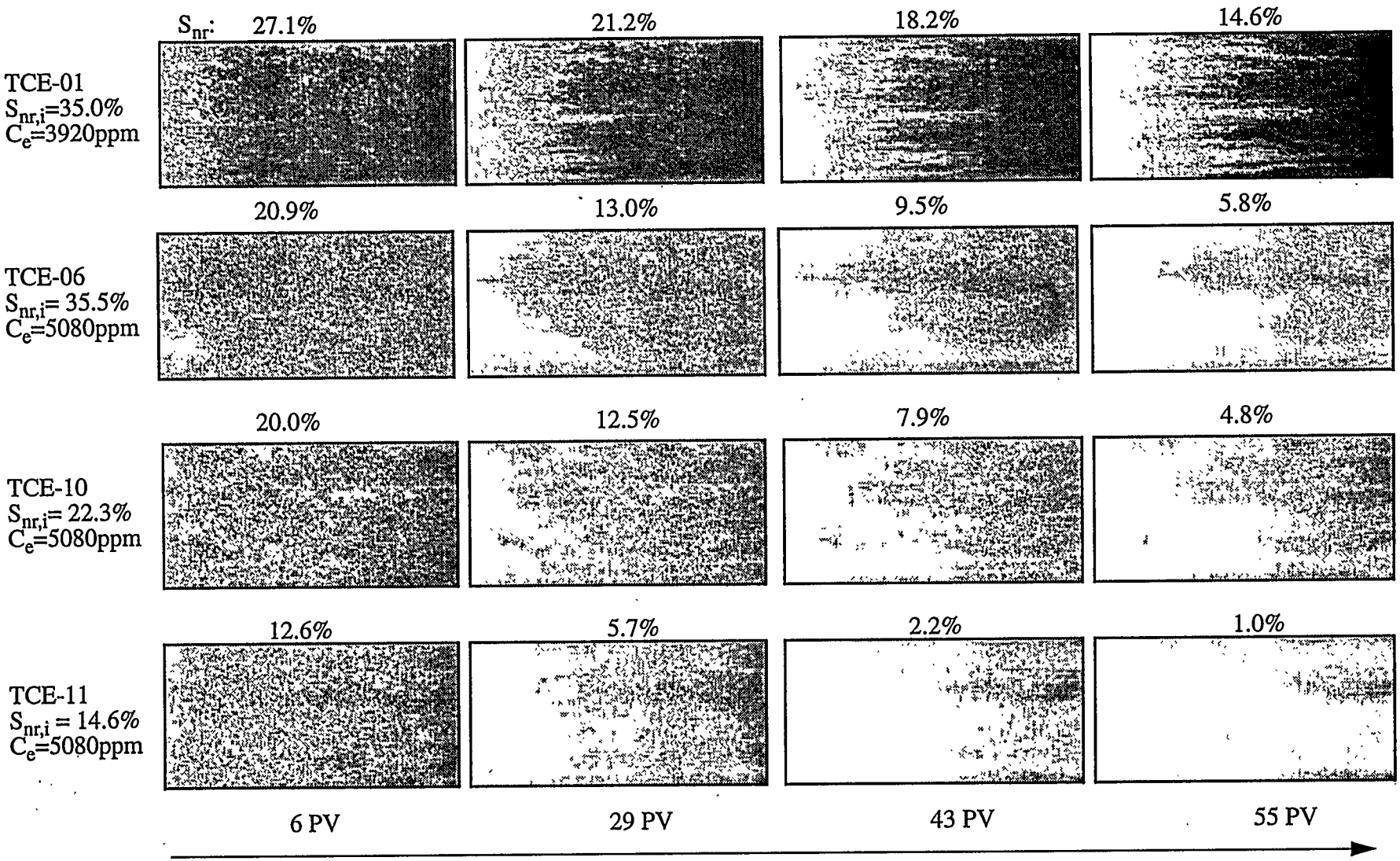
S_{nr}: 27.1%
21.2%
18.2%
14.6%
TCE-01
$S_{nr,i}$=35.0%
C_e=3920ppm
20.9%
13.0%
9.5%
5.8%
TCE-06
$S_{nr,i}$= 35.5%
C_e=5080ppm
20.0%
12.5%
7.9%
4.8%
TCE-10
$S_{nr,i}$= 22.3%
C_e=5080ppm
12.6%
5.7%
2.2%
1.0%
TCE-11
$S_{nr,i}$ = 14.6%
C_e=5080ppm
6 PV
29 PV
43 PV
55 PV

Fig. 13

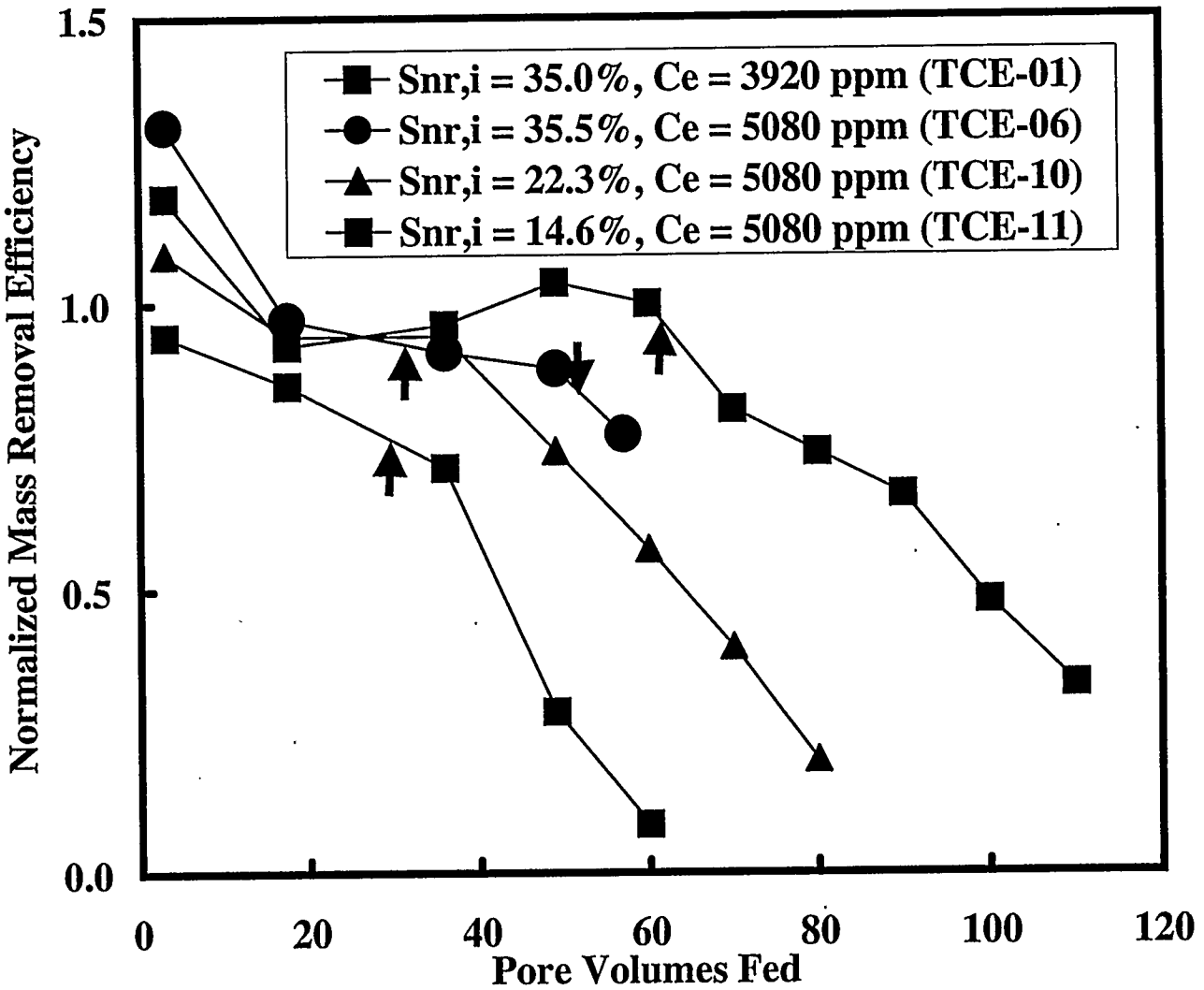
Snr,i = 35.0%, Ce = 3920 ppm (TCE-01)
Snr,i = 35.5%, Ce = 5080 ppm (TCE-06)
Snr,i = 22.3%, Ce = 5080 ppm (TCE-10)
Snr,i = 14.6%, Ce = 5080 ppm (TCE-11)
Normalized Mass Removal Efficiency
1.5
1.0
0.5
0.0
0
20
40
60
80
100
120
Pore Volumes Fed

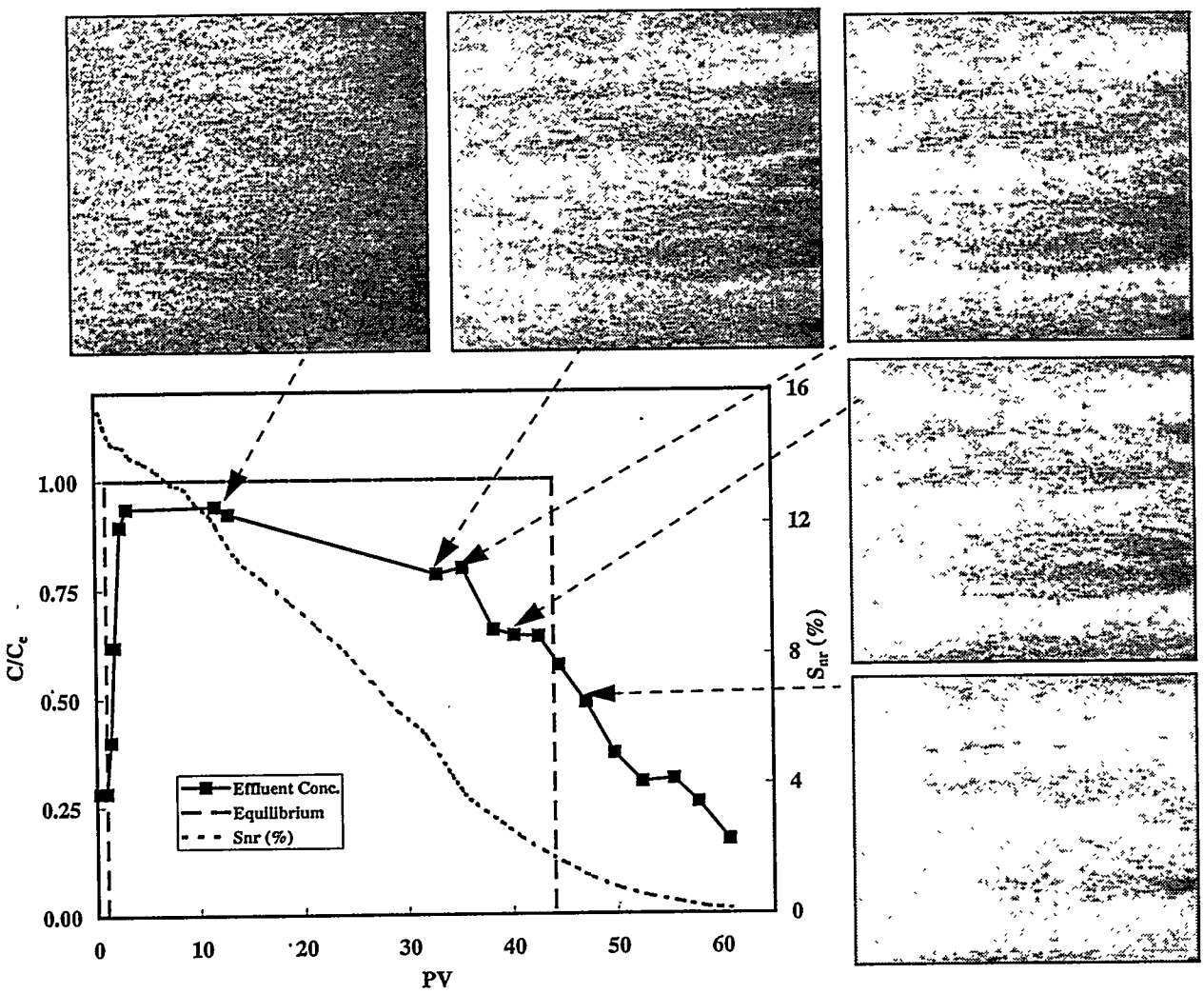
1.00
0.75
0.50
0.25
0.00
C/Ce
0
10
20
30
40
50
60
PV
16
12
8
4
0
Snr (%)
Effluent Conc.
Equilibrium
Snr (%)

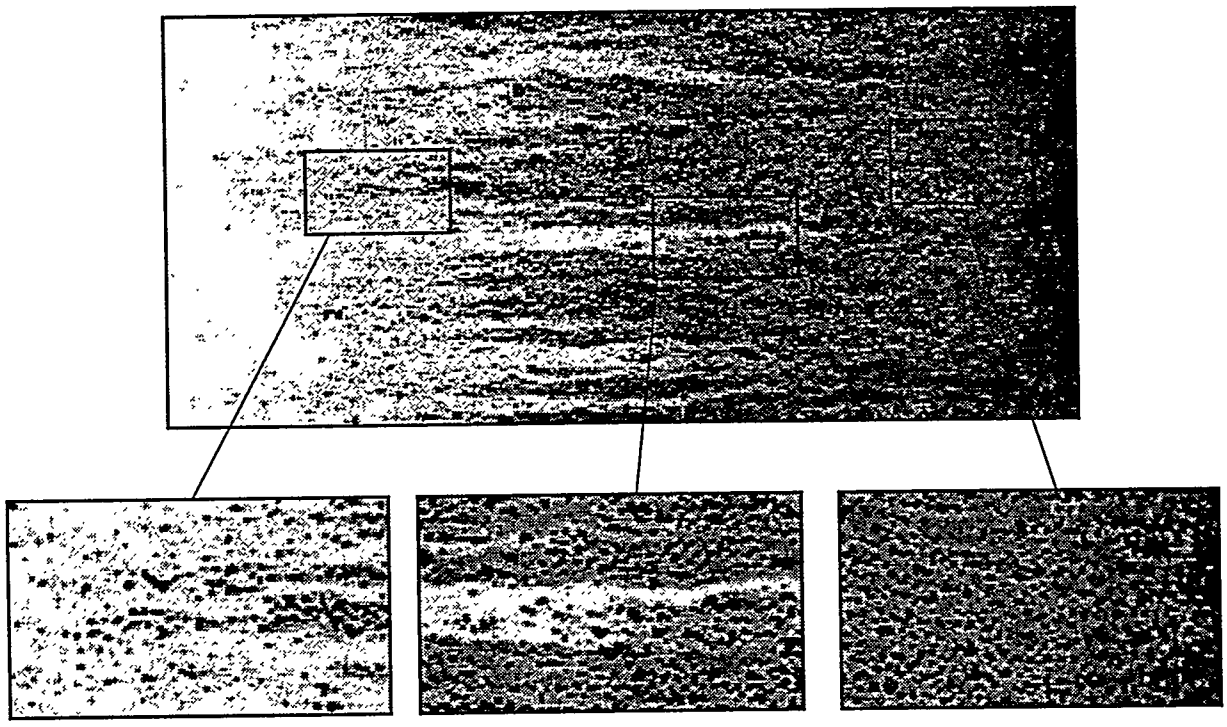

Fig. 16